The JCMT Gould Belt Survey: first results from the SCUBA-2 observations of the Ophiuchus molecular cloud and a virial analysis of its prestellar core population

K. Pattle,[1]★ D. Ward-Thompson,[1] J. M. Kirk,[1] G. J. White,[2,3] E. Drabek-Maunder,[4]
J. Buckle,[5,6] S. F. Beaulieu,[7] D. S. Berry,[8] H. Broekhoven-Fiene,[9] M. J. Currie,[8]
M. Fich,[7] J. Hatchell,[10] H. Kirk,[11] T. Jenness,[8,12] D. Johnstone,[8,11,9] J. C. Mottram,[13]
D. Nutter,[14] J. E. Pineda,[15,16,17] C. Quinn,[14] C. Salji,[5,6] S. Tisi,[7] S. Walker-Smith,[5,6]
J. Di Francesco,[11,9] M. R. Hogerheijde,[13] Ph. André,[18] P. Bastien,[19] D. Bresnahan,[1]
H. Butner,[20] M. Chen,[9] A. Chrysostomou,[21] S. Coude,[19] C. J. Davis,[22]
A. Duarte-Cabral,[10] J. Fiege,[23] P. Friberg,[8] R. Friesen,[24] G. A. Fuller,[16] S. Graves,[5,6]
J. Greaves,[25] J. Gregson,[2,3] M. J. Griffin,[14] W. Holland,[26,27] G. Joncas,[28]
L. B. G. Knee,[11] V. Könyves,[18,29] S. Mairs,[9] K. Marsh,[14] B. C. Matthews,[11,9]
G. Moriarty-Schieven,[11] J. Rawlings,[30] J. Richer,[5,6] D. Robertson,[31] E. Rosolowsky,[32]
D. Rumble,[10] S. Sadavoy,[33] L. Spinoglio,[34] H. Thomas,[8] N. Tothill,[35] S. Viti,[30]
J. Wouterloot,[8] J. Yates[30] and M. Zhu[36]

Affiliations are listed at the end of the paper

ABSTRACT

In this paper, we present the first observations of the Ophiuchus molecular cloud performed as part of the James Clerk Maxwell Telescope (JCMT) Gould Belt Survey (GBS) with the SCUBA-2 instrument. We demonstrate methods for combining these data with previous HARP CO, *Herschel*, and IRAM N_2H^+ observations in order to accurately quantify the properties of the SCUBA-2 sources in Ophiuchus. We produce a catalogue of all of the sources found by SCUBA-2. We separate these into protostars and starless cores. We list all of the starless cores and perform a full virial analysis, including external pressure. This is the first time that external pressure has been included in this level of detail. We find that the majority of our cores are either bound or virialized. Gravitational energy and external pressure are on average of a similar order of magnitude, but with some variation from region to region. We find that cores in the Oph A region are gravitationally bound prestellar cores, while cores in the Oph C and E regions are pressure-confined. We determine that N_2H^+ is a good tracer of the bound material of prestellar cores, although we find some evidence for N_2H^+ freeze-out at the very highest core densities. We find that non-thermal linewidths decrease substantially between the gas traced by $C^{18}O$ and that traced by N_2H^+, indicating the dissipation of turbulence at higher densities. We find that the critical Bonnor–Ebert stability criterion is not a good indicator of the boundedness of our cores. We detect the pre-brown dwarf candidate Oph B-11 and find a flux density and mass consistent with previous work. We discuss regional variations in the nature of the cores and find further support for our previous hypothesis of a global evolutionary gradient across the cloud from south-west to north-east, indicating sequential star formation across the region.

Key words: stars: formation – dust, extinction – ISM: individual objects: L1688 – ISM: individual objects: L1689 – ISM: kinematics and dynamics – submillimetre: ISM.

★ E-mail: kpattle@uclan.ac.uk

1 INTRODUCTION

The Ophiuchus molecular cloud is a nearby (139 ± 6 pc; Mamajek 2008), well-studied (Wilking et al. 2008), site of low-mass star formation (Wilking & Lada 1983). It consists of two submillimetre-bright central regions, L1688 and L1689, each of which has extensive filamentary streamers (see e.g. Loren 1989). Ophiuchus is considered to be the nearest site of clustered star formation (Wilking & Lada 1983; Motte, André & Neri 1998). Star formation in Ophiuchus is heavily influenced by the nearby Sco OB2 association (Vrba 1977), the centre of which is at a distance of 11 ± 3 pc from Ophiuchus (Mamajek 2008). The south-west/north-east-aligned filamentary streamers from each of the central regions are thought to be due to the effects of this association (Vrba 1977; Loren 1989). The L1688 cloud shows a much more active star formation history than the neighbouring L1689 cloud to the east, supporting this scenario (Nutter, Ward-Thompson & André 2006, hereafter NWA06).

Ophiuchus is a part of the Gould Belt, a ring of molecular clouds and OB associations $\sim$1 kpc in diameter and inclined $\sim$20° to the Galactic Plane (Herschel 1847; Gould 1879). The Gould Belt is considered a 'laboratory' for the study of low-mass star formation, as most of the low-mass star-forming regions within 500 pc of the Earth are associated with it. This has led to surveys aimed at mapping substantial fractions of the Gould Belt being undertaken using the JCMT (Ward-Thompson et al. 2007), the *Herschel* Space Observatory (André et al. 2010), and the *Spitzer* Space Telecope (Evans et al. 2009).

In this paper, we report on the Submillimetre Common-User Bolometer Array 2 (SCUBA-2) first results for Ophiuchus from the JCMT Gould Belt Survey (GBS)[1] and compare them to Heterodyne Array Receiver Program (HARP) CO $J = 3$–2 observations from the JCMT GBS, as well as to data from other GBSs. We study the starless core population of Ophiuchus, in particular investigating the stability of the cores against gravitational collapse in order to identify the prestellar (i.e. gravitationally bound; Ward-Thompson et al. 1994) subset of the population of starless cores. There have been many previous wide-field millimetre and submillimetre studies of the starless core population in the L1688 cloud (e.g. Motte et al. 1998, hereafter MAN98; Johnstone et al. 2000; Enoch et al. 2008; Simpson, Nutter & Ward-Thompson 2008, hereafter S08; Simpson et al. 2011).

This paper is laid out as follows: in Section 2, we discuss the observations and data reduction. In Section 3, we discuss data processing, including techniques for combining SCUBA-2 and *Herschel* data. In Section 4, we present our catalogue of sources, discussing source extraction and characterization of sources using continuum and line data. In Section 5, we discuss the energy balance and stability of the starless cores among our sources. In Section 6, we discuss how the properties of our starless cores vary with region. Section 7 summarizes the conclusions of this paper.

2 OBSERVATIONS

2.1 SCUBA-2

The SCUBA-2 (Holland et al. 2013) observations presented here form part of the JCMT GBS (Ward-Thompson et al. 2007). Continuum observations at 850 and 450 µm were made using fully sampled 30 arcmin diameter circular regions (PONG1800 mapping mode;

Bintley et al. 2014) at resolutions of 14.1 and 9.6 arcsec, respectively. Larger regions were mosaicked with overlapping scans. The new SCUBA-2 data are shown in Figs 1 and 2, for the regions of the map with significant emission. The full maps, along with the variance arrays, are shown in Figs A1–A4 in Appendix A.

The data were reduced using an iterative map-making technique (*makemap* in SMURF; Chapin et al. 2013), and gridded to 6 arcsec pixels at 850 µm and 4 arcsec pixels at 450 µm, as part of the Internal Release 1 GBS data set. The iterations were halted when the map pixels, on average, changed by <0.1 per cent of the estimated map rms. The initial reductions of each individual scan were co-added to form a mosaic from which a mask based on signal-to-noise ratio (SNR) was produced for each region. The final mosaic was produced from a second reduction using this mask to define areas of emission. Detection of emission structure and calibration accuracy are robust within the masked regions, and are uncertain outside of the masked region. The mask used in the reduction can be seen in Fig. A5 in Appendix A.

A spatial filter of 10 arcmin is used in the reduction, which means that flux recovery is robust for sources with a Gaussian full width at half-maximum (FWHM) less than 2.5 arcmin. Sources between 2.5 and 7.5 arcmin in size will be detected, but both the flux and the size are underestimated because Fourier components with scales greater than 5 arcmin are removed by the filtering process. Detection of sources larger than 7.5 arcmin is dependent on the mask used for reduction. The mask introduces further spatial filtering, as after all but the final iteration of the map-maker, all emission outside the region enclosed by the mask is suppressed. The recovery of extended structure outside of the masked regions (shown in Fig. A5 in Appendix A) is limited.

The data are calibrated in Jy pixel^{-1}, using aperture flux conversion factors of 2.34 and 4.71 Jy pW^{-1} arcsec^{-2} at 850 and 450 µm, respectively, derived from average values of JCMT calibrators (Dempsey 2013), and correcting for the pixel area. The PONG scan pattern leads to lower noise levels in the map centre and overlap regions, while data reduction and emission artefacts can lead to small variations in the noise level over the whole map.

Four overlapping subsections of the L1688 region were each observed four times between 2012 May 6 and 2012 July 4 in very dry (Grade 1; $\tau_{225\,\mathrm{GHz}} < 0.05$) weather. Three overlapping subsections of the L1689 region were each observed six times between 2012 June 10 and 2013 June 30 in dry (Grade 2; $\tau_{225\,\mathrm{GHz}} < 0.08$) weather. One section of the L1709 region was observed six times in Grade 2 weather between 2013 July 18 and 27, as was one section of the L1712 region between 2013 July 28 and 29. We found a typical 1σ noise level of 1.73 mJy 6 arcsec^{-1} pixel in the 850-µm SCUBA-2 data and 14.9 mJy 4 arcsec^{-1} pixel in the 450-µm SCUBA-2 data.

2.2 HARP

The HARP (Buckle et al. 2009) receiver contains an array of 16 heterodyne detectors, arranged in a 4 × 4 footprint on the sky. HARP is used in conjunction with the Auto-Correlation Spectrometer and Imaging System (ACSIS; Buckle et al. 2009) backend. The L1688 region of Ophiuchus was observed as part of the JCMT GBS (Ward-Thompson et al. 2007), in three isotopologues of the CO $J = 3$–2 transition: ^{12}CO, ^{13}CO, and C^{18}O, at a resolution of 14 arcsec. These data are presented elsewhere (White et al. 2015). The region of the SCUBA-2 map for which ^{12}CO data are available (an area approximately 2050 arcsec×2500 arcsec, centred on L1688) is outlined in red on Fig. 1, while the region for which both ^{13}CO
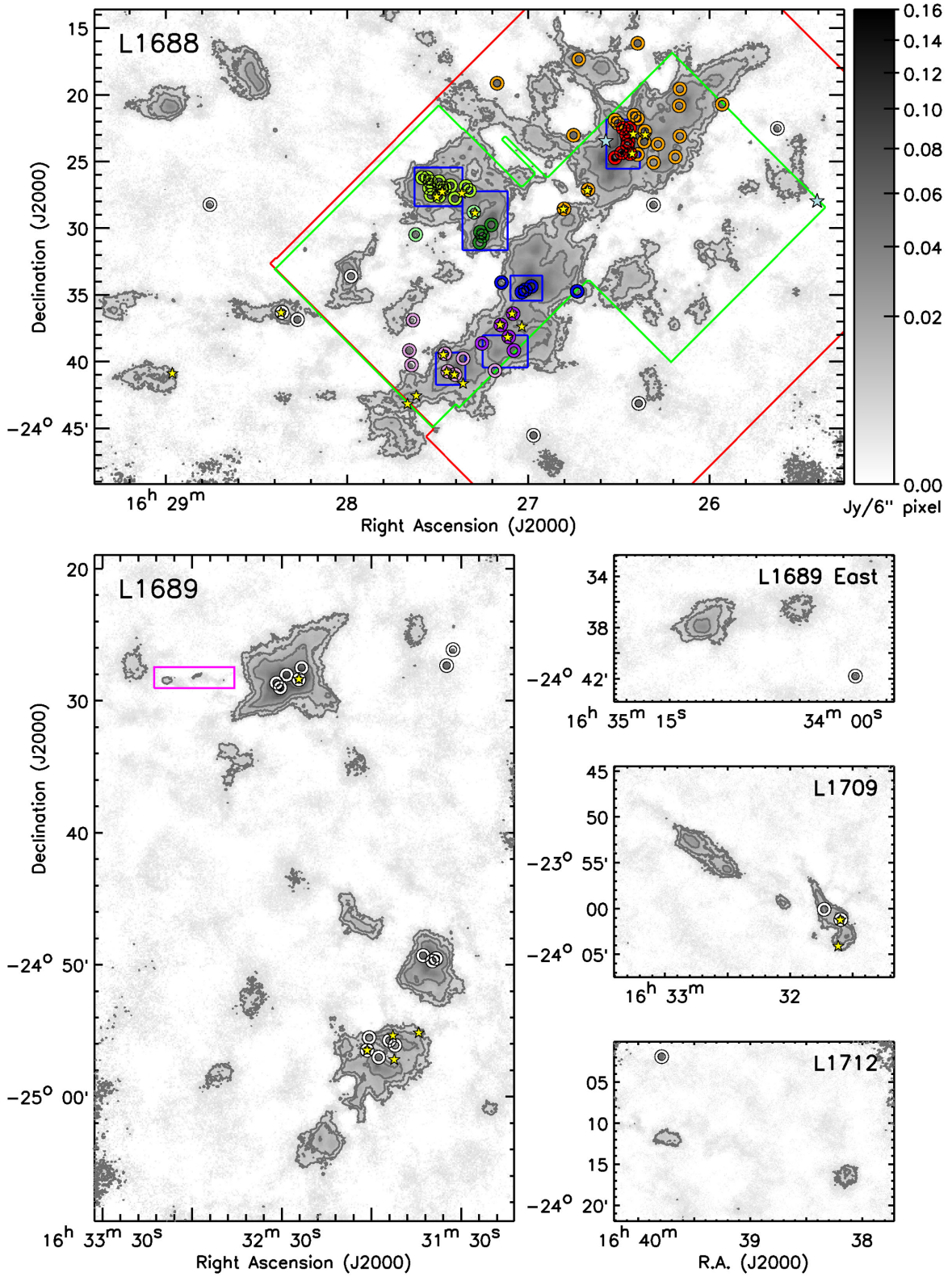
Figure 1. 850-μm flux density data, shown in square-root scaling, for each of the subregions of Ophiuchus (see text for details). ^{12}CO data are available in the area outlined in red; ^{13}CO and $C^{18}O$ data are available in the area outlined in green; N_2H^+ data are available in the areas outlined in blue. The CO outflow associated with IRAS 16293−2422 is marked in magenta. Open circles mark the sources we extract from the 850 μm data (see text for details of colour coding). Yellow stars mark the embedded protostars (Enoch et al. 2009). Blue stars mark the B stars HD 147889 and S1.
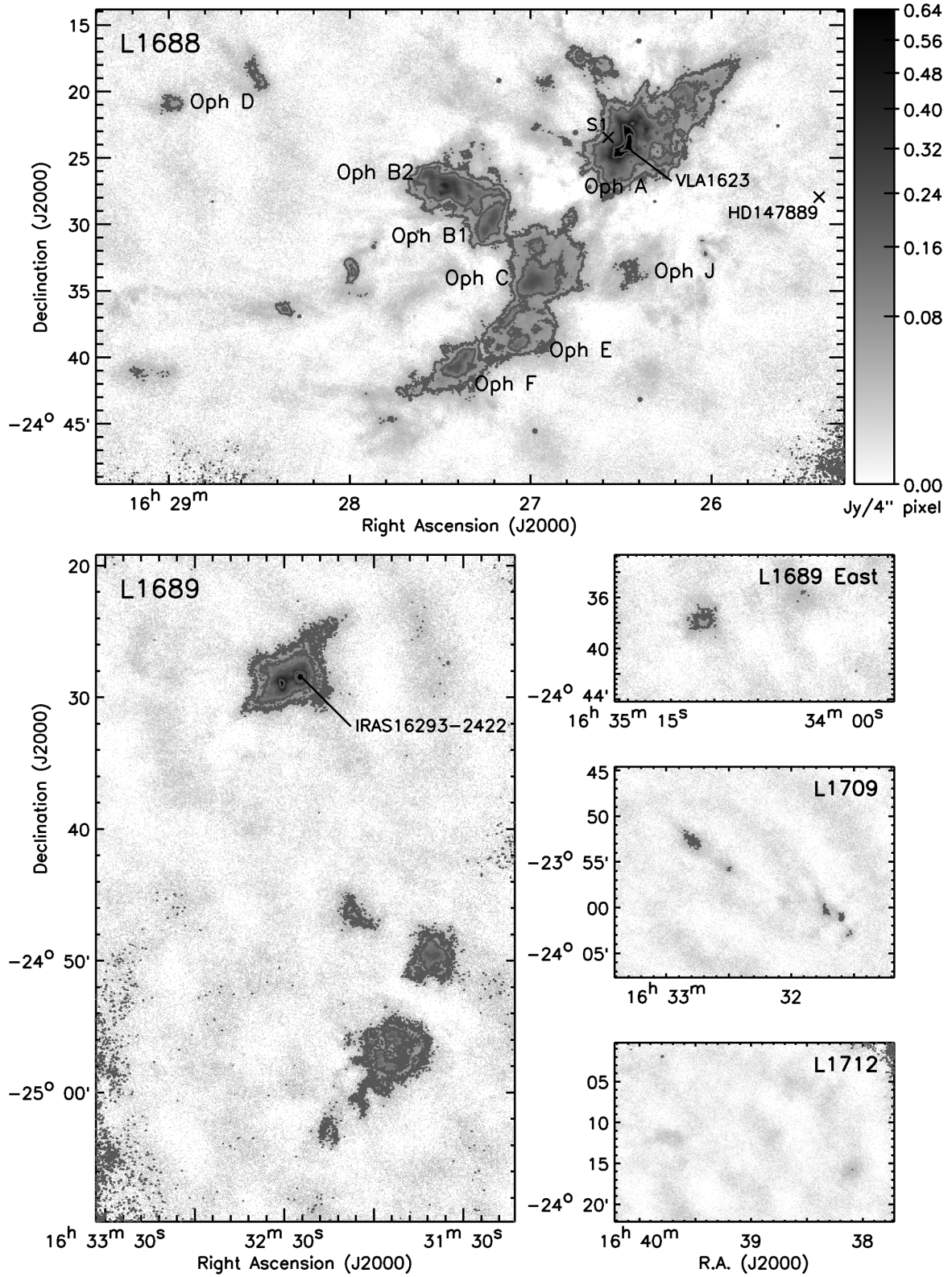
Figure 2. 450-μm flux density data, shown in square-root scaling, for each of the subregions of Ophiuchus (see text for details). The B stars HD 147889 and S1 are marked, along with the Class 0 protostars VLA 1623 and IRAS 16293−2422. The subregions of the L1688 cloud are labelled.

and C^{18}O data are available (two overlapping regions, each with an area approximately 1000 arcsec × 1000 arcsec) is outlined in green.

2.3 *Herschel* Space Observatory

The *Herschel* Space Observatory was a 3.5m-diameter telescope, which operated in the far-infrared and submillimetre regimes (Pilbratt et al. 2010). The observations for this paper were taken simultaneously with the Photodetector Array Camera and Spectrometer, PACS (Poglitsch et al. 2010), and the Spectral and Photometric Imaging Receiver, SPIRE (Griffin et al. 2010; Swinyard et al. 2010) using the combined fast-scanning (60 arcsec s^{-1}) SPIRE/PACS parallel mode. Of these data sets, we used the three highest resolution: PACS 70 μm, at 6 arcsec × 12 arcsec; PACS 160 μm, at 12 arcsec × 16 arcsec and SPIRE 250 μm, at 18 arcsec. The data used in this paper were taken as part of the *Herschel* Gould Belt Survey – hereafter HGBS (André et al. 2010). HGBS Ophiuchus data are presented elsewhere (Roy et al. 2014; Ladjelate et al., in preparation). We use them here for comparison with the SCUBA-2 data. These data, with Observation IDs 1342205093 and 1342205094, were reduced using HIPE version 5.1. The SCUBA-2 pipeline was applied to the *Herschel* observations in order to make the data sets comparable, as discussed in Section 3.2. This process removes large-scale structure from the *Herschel* observations, removing the necessity of applying background-correction offsets to the *Herschel* observations.

2.4 IRAM

Archival N$_2$H$^+$ $J = 1$–0 data are also used (Di Francesco, André & Myers 2004; André et al. 2007). These observations were carried out with the Institut de Radioastronomie Millimétrique (IRAM) 30-m telescope at Pico Veleta, Spain, in 1998 June, 2000 July, and 2005 June. The FWHM of the IRAM beam at 3 mm is ~26 arcsec. For the purposes of improving SNR, we binned the data to a 15 arcsec pixel grid. The regions of the area mapped with SCUBA-2 for which IRAM data are available are outlined in blue on Fig. 1.

3 DATA PROCESSING

Figs 1 and 2 show the new SCUBA-2 data. Figs B1 and B2 in Appendix B show the SCUBA-2 data compared to the *Herschel* data.

3.1 CO contamination

SCUBA-2 850 μm data may be substantially contaminated by the CO $J = 3$–2 transition (Drabek et al. 2012) which, with a rest wavelength of 867.6 μm, is covered by the SCUBA-2 850 μm filter, which has a half-power bandwith of 85 μm (Holland et al. 2013). Drabek et al. (2012) estimate that the contribution to the measured 850-μm continuum emission from CO is generally ≤20 per cent, but can reach ~80 per cent in outflow-dominated regions. Some CO contamination in the 850 μm data is expected for L1688, primarily due to the bright and extended outflow from the Class 0 protostar VLA1623 (André, Ward-Thompson & Barsony 1993).

In this region, CO contamination was corrected for by re-reducing each of the 850 μm observations with the integrated ^{12}CO data added to the SCUBA-2 bolometer time series as a negative signal. The contribution of CO emission to the total observed flux density in L1688 was found to be 4.6 per cent. The fractional CO contamination varies significantly across L1688. In the dense centres of Oph A, B, C, and F the CO contamination fraction is typically

<1 per cent, while in Oph E, located along the same line of sight as the edge of the outflow from VLA 1623, the contamination reaches up to 10 per cent. However, in the brightest regions of CO emission from the outflow from VLA 1623 and the PDR associated with HD 147889 – both regions of low 850-μm continuum emission – the contamination fraction reaches ~100 per cent. HARP CO data are only available for the central L1688 region; other regions cannot be corrected for in the same manner. However, it is only in L1688 that there is likely to be substantial contamination, and as even in L1688 the mean contribution of the CO emission is less than 5 per cent, dropping to <1 per cent in the dense, 850-μm bright regions in which the majority of our sources lie, it is unlikely that measured 850-μm flux densities outside of this region are significantly affected.

As a caveat, we note that a CO outflow can be seen in the 850 μm data of L1689, to the east of the northernmost part of the region. This outflow, marked in magenta on Fig. 1, was previously identified as submillimetre condensation SMM 21 by NWA06, and is likely to be the outflow known to be associated with the protostar(s) IRAS 16293−2422 (Mizuno et al. 1990). This indicates that there is likely to be some CO contamination associated with IRAS 16293−2422 in the L1689 north region. Flux densities, and hence masses, in this region may be overestimated as a result.

3.2 Spatial filtering

SCUBA-2 is not sensitive to spatial scales greater than 600 arcsec. In order to make SCUBA-2 and *Herschel* observations comparable, the large-scale structure must be removed from the *Herschel* observations. To accomplish this, the SCUBA-2 pipeline was applied to the *Herschel* observations following the method described by Sadavoy et al. (2013), in which the *Herschel* data are added to the SCUBA-2 bolometer time series, and the reduction process, as described in Section 2.1, is repeated, including the application of the mask shown in Fig. A5 to the *Herschel* data. The original SCUBA-2 reduction of the data is then subtracted from the *Herschel*+SCUBA-2 map, leaving the spatially-filtered *Herschel* signal. The aim of this procedure is to treat the *Herschel* data as if it were SCUBA-2 data. In order to achieve this, it is necessary to minimize the effect of the *Herschel* data on the map-making process by treating it as a small perturbation to the SCUBA-2 signal (the input *Herschel* data are scaled appropriately). In this way, differences in areas of significant emission, noise levels and beam size between the SCUBA-2 and *Herschel* maps do not distort the final, filtered, map, or prevent the map-making process from converging.

This spatial filtering removes the need to use *Planck* data to determine global background levels for the *Herschel* data sets (see e.g. Planck VI 2011), as all large-scale structure is removed from the filtered maps, leaving no background signal in emission-free regions. The filtering process was repeated once for each SCUBA-2 observing position for which there was corresponding *Herschel* data, and the resulting spatially-filtered maps were combined to form a mosaic. The only region in the SCUBA-2 mosaic of Ophiuchus not covered by *Herschel* is L1712.

3.3 Common-resolution convolution kernels

SCUBA-2 450-μm flux densities have previously been seen to show an excess over the values predicted from interpolation of the *Herschel* 350 and 500 μm bands (Sadavoy et al. 2013). This discrepancy was also seen in our data when they were brought to a common resolution using the published beam models. The hypothesis that

the apparent 450 μm excess was caused by the approximation of the SCUBA-2 450-μm beam secondary component as a Gaussian (Dempsey et al. 2013) led to the construction of a set of convolution kernels from the *Herschel* and SCUBA-2 beam maps following the method of Aniano et al. (2011), which we summarize here. This method works from beam maps rather than published beam models, and involves constructing a convolution kernel $K(A{\Rightarrow}B)$ that maps point spread function (PSF) A on to the lower resolution PSF B:

$$\mathrm{PSF}_B = K(A \Rightarrow B) * \mathrm{PSF}_A. \tag{1}$$

In principle, $K(A{\Rightarrow}B)$ is derived using

$$K(A \Rightarrow B) = \mathrm{FT}^{-1}\left(\frac{\mathrm{FT}(\mathrm{PSF}_B)}{\mathrm{FT}(\mathrm{PSF}_A)}\right), \tag{2}$$

where FT represents the Fourier Transform operator and FT^{-1} the inverse Fourier transform. However, in practice the division by $\mathrm{FT}(\mathrm{PSF}_A)$ leads to $K(A{\Rightarrow}B)$ being dominated by noise, unless the high spatial frequency (i.e. high wavenumber k) components of PSF A are filtered. First, high-frequency noise is filtered from both PSFs using a filter ϕ which takes the form

$$\phi(k) = \begin{cases} 1 & \text{for } k \le k_\alpha \\ \exp\left[-\left(1.8249 \times \frac{k-k_\alpha}{k_\beta-k_\alpha}\right)^4\right] & \text{for } k_\alpha < k \le k_\beta \\ 0 & \text{for } k_\beta < k \end{cases} \tag{3}$$

where $k_\alpha = 0.9k_\beta$ and $k_\beta = 8\pi/\mathrm{FWHM}$ where FWHM is the FWHM of the instrument primary beam. Hereafter, $\mathrm{FT}_\phi = \phi \times \mathrm{FT}$. The highest-frequency components of PSF A are further filtered: equation (2) becomes

$$K(A \Rightarrow B) = \mathrm{FT}^{-1}\left(\frac{\mathrm{FT}_\phi(\mathrm{PSF}_B)}{\mathrm{FT}_\phi(\mathrm{PSF}_A)} \times f_A\right), \tag{4}$$

and the filter f_A takes the form

$$f_A(k) = \begin{cases} 1 & \text{for } k \le k_{\mathrm{L,A}} \\ \frac{1}{2}\left[1 + \cos\left(\pi \times \frac{k-k_{\mathrm{L,A}}}{k_{\mathrm{H,A}}-k_{\mathrm{L,A}}}\right)\right] & \text{for } k_{\mathrm{L,A}} < k \le k_{\mathrm{H,A}} \\ 0 & \text{for } k_{\mathrm{H,A}} < k \end{cases} \tag{5}$$

where $k_{\mathrm{H,A}}$ is the highest wavenumber at which $\mathrm{FT}(\mathrm{PSF}_A)$ is appreciable:

$$\mathrm{FT}(\mathrm{PSF}_A)(k_{\mathrm{H,A}}) = 0.005 \times \mathrm{FT}(\mathrm{PSF}_A)_{\mathrm{max}}, \tag{6}$$

and $k_{\mathrm{L,A}} = 0.7k_{\mathrm{H,A}}$. Prior to constructing the convolution kernel, the PSFs are centroided, resampled to a common grid of 3645×3645 0.2 arcsec pixels, and circularly averaged. The SCUBA-2 and SPIRE beams are already approximately circular and are largely unchanged by this circular averaging. The PACS beam, which is substantially elliptical, is more affected, and the convolution process may produce some slight distortion in the convolved 160 μm map. However, as both the circular averaging process and the convolution process conserve flux, and as the PACS 160 μm beam (12 arcsec × 16 arcsec) is smaller than the SPIRE 250 μm beam (18 arcsec) along both its major and minor axes, the total flux measured inside each aperture at 160 μm will be accurate. It should also be noted that all of the SCUBA-2, SPIRE, and PACS instruments scan in more than one direction on the sky while taking an observation, and hence the beam pattern is rotated several times within each observation. This means that the beam pattern is to some extent circularly averaged even before the convolution is applied.

Fig. 3 shows the result of convolving the maps with these kernels to the lowest resolution wavelength band being considered (*Herschel* 250 μm); this caused a marked reduction in the discrepancy
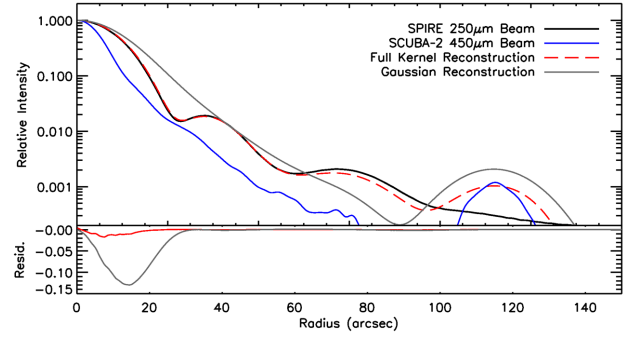

Figure 3. Convolution of the SCUBA-2 450 μm beam (blue) to the *Herschel* 250 μm beam (black). The red dashed line shows the result of the convolution kernel, while the grey solid line shows the result of convolution by a Gaussian beam model.

between the 450-μm flux density and the *Herschel* flux densities. This then allowed the 450 μm data to be used in spectral energy distribution (SED) fitting, as discussed below.

4 RESULTS

4.1 Source extraction

Source extraction was performed on the CO-subtracted SCUBA-2 850 μm map of L1688, and the non-CO-subtracted SCUBA-2 850 μm map of the remainder of the field. Sources were identified using the curvature-based CuTEx algorithm (Molinari et al. 2011) in its detection mode. CuTEx identifies sources through signal in the second derivatives of the input map, effectively removing background and large-scale structure from the map, and leaving the sharp changes in gradient associated with compact sources. CuTEx was chosen after extensive testing of various different methods as the algorithm best able to break apart the emission in crowded regions of the map (Oph A and Oph B), and which was in the most agreement with previous studies.

CuTEx identified 70 sources in the CO-subtracted L1688 region and 23 sources in the rest of the observed field: four in the remainder of L1688, seven in L1689 north, eight in L1689 south, one in L1689 east, two in L1709, and one in L1712. All but one of our sources are within the masked areas described in Section 2.1 and shown in Fig. A5. Source 74/L1688N SMM 1, which lies outside the mask, is the known protostellar object DoAr 4 (see Table 2 and discussion on source classification below).

Of the 70 sources in the CO-subtracted L1688 region, 46 were uniquely associated with a source in the S08 catalogue. A source is considered to be uniquely identified in the S08 catalogue if its FWHM area overlaps with that of an S08 source, and if it is the only source in our catalogue to do so. The S08 catalogue identifies 93 sources in SCUBA observations of L1688, of which 91 are within the CO-subtracted SCUBA-2 field. In Oph A, all of our sources have a unique counterpart in the S08 catalogue. In Oph B2, we identify 13 sources while S08 identify 12. The discrepancies between the two catalogues are mostly in low signal-to-noise regions and are likely to be due in part to the different source-finding criteria used (see discussion on completeness in Section 4.2).

Of the 16 sources in L1689, 13 were uniquely identified sources in the NWA06 catalogue, while the remaining 3 sources were substructure within NWA06 SMM 16.

The sources identified by CuTEx were characterized using a custom multiple-Gaussian fitting code, which models the flux density

of sources in crowded regions by fitting a 2D Gaussian to each of a set of associated sources simultaneously. This method uses the source positions and sizes provided by CuTEx as initial input to the fitting routine *mpfit* (Markwardt 2009), along with the model:

$$F(x, y) = a + bx + cy + \sum_{n=1}^{N} A_n e^{-\frac{1}{2}\left(\left(\frac{x'_n}{\sigma_{x,n}}\right)^2 + \left(\frac{y'_n}{\sigma_{y,n}}\right)^2\right)}, \quad (7)$$

where

$$x'_n = (x - x_{0,n})\cos(\theta_n) - (y - y_{0,n})\sin(\theta_n) \quad (8a)$$

$$y'_n = (x - x_{0,n})\sin(\theta_n) + (y - y_{0,n})\cos(\theta_n), \quad (8b)$$

and N is the number of sources to be fitted simultaneously.

Sources are considered to be neighbours if they are separated by less than twice the FWHM of the larger source. Groups to be fitted simultaneously are defined such that each source in a group is a neighbour to at least one other source in the group, and no source has any neighbours outside of the group, with isolated sources considered as being in a one-member group. For each group, the local background is fitted as an inclined plane with coefficients a, b, and c, while for each Gaussian, the quantities A, peak flux density, x_0 and y_0, central coordinates, σ_x and σ_y, semimajor and semiminor axes, and θ, position angle, are fitted. In order to accurately fit $6N + 3$ parameters for each group, *mpfit* was constrained such that for each source, $A > 0$, Δx_0 and $\Delta y_0 \leq 6$ arcsec, $\Delta\sigma_x$ and $\Delta\sigma_y \leq 10$ per cent, and $\Delta\theta \leq 5°$, where Δ signifies the amount that the quantity is allowed to vary from its initial value supplied by CuTEx. The fitted quantities do not hit the borders of the allowed parameter space. CuTEx detects signal in the second derivatives of the input map, and hence can determine source sizes and orientations accurately, as it is sensitive to changes in gradient.

Our sources are listed in Table 1. In L1688, we continue the naming convention introduced by MAN98 and used by S08, while in L1689 we continue the naming convention of NWA06. For each source, we list: the index of the source; the name of the source using the official IAU naming convention; the name by which we refer to the source in the text; central right ascension and declination; position angle of the ellipse fitted to the source measured east of north; major and minor FWHMs; best-fitting model peak 850 μm flux density and total 850-μm flux density of the background-subtracted source; whether the source has associated emission in the *Herschel* 70 μm data (a listing of 'S1' indicating that the IR emission at the source location is likely to be due to the reflection nebula associated with the star S1); our evaluation of whether the source is starless or protostellar ('C' indicating a starless core and 'P' indicating a protostellar source; classification criteria and question-marked sources are discussed below); the source's identity in the S08 or NWA06 catalogues (if relevant); and the region in which the source is located. Our sources are marked on Fig. 1 as open circles, coloured according to region: red for the central Oph A region, (defined as the region contiguous with the prestellar source SM1 where $F_{\nu(850\,\mu m)}^{peak} > 0.6$ Jy 6 arcsec pixel^{-1}); orange for the more diffuse material around Oph A, hereafter referred to as Oph A′; dark green for Oph B1; light green for Oph B2; blue-green for the intermediate region Oph B1B2; blue for Oph C; dark purple for Oph E; light purple for Oph F; and white for all other regions. This identification of region by colour is used throughout the rest of this paper, except that cores marked in white in Fig. 1 are elsewhere marked in black.

We judge a source as being a starless core or protostellar by considering whether its morphology appears to be point-like or ex-

tended at 850 μm, whether it has associated 70 μm emission (see e.g. Könyves et al. 2010), and the shape of its SED. The first two criteria are of the most importance, as in principle a protostellar source detectable at 850 μm should have a point-like morphology at both 850 and 70 μm. The SED shape should then confirm the identification. However, in practice, each of these criteria has limitations. While a point-like morphology is a good indicator of an unresolved protostellar source, an extended morphology at 850 μm does not preclude the presence of a protostar, deeply embedded or otherwise confused with emission from cold gas along the same line of sight. Extended emission from warm gas may confuse identification of protostars by the presence of 70 μm emission at their position, particularly in the reflection nebula associated with the star S1 (70 μm associations likely to be caused by this reflection nebula are noted in Table 1). Similarly, a rising SED at short wavelengths indicates a high-temperature object, possibly a protostellar envelope, but may also be caused by the presence of warm material along the line of sight not directly associated with the source. In order to clarify these identifications, we also investigated whether there is a previously-identified protostar present within one 850-μm JCMT beam size (14.1 arcsec) of each of our source positions. This criterion was generally used only to confirm the identification made using the observational criteria listed above. However, in some cases it became necessary to use the presence or absence of a previously-identified protostar as the deciding criterion when classifying a source, particularly in crowded regions with substantial IR contamination. Previously-known protostars were located using the SIMBAD astronomical data base (Wenger et al. 2000). Those sources we identify as protostellar are listed in Table 2, with alternative identifications and, where known, their evolutionary class. Source 93/L1712 SMM 1, for which *Herschel* data are not available, was catagorized as protostellar based on its 850-μm morphology and identification with the protostar IRAS 16367−2356 (see Table 2).

For the majority of our sources, a consistent classification can be made from each of our criteria. However, where this is not the case, our classifications in Table 1 are followed by question marks. In the case of a 'C?' listing, this indicates that while all other criteria suggest that this is a starless core, there is some 70 μm emission at the location of the source. In the case of a 'P?' listing, this indicates that while the source can be identified with a known protostar, one or more of the selection criteria – typically, a non-point-like morphology – suggests that the source might be extended. A queried classification indicates a slight conflict between our classification criteria, rather than substantial doubt about the nature of the source.

Hereafter, 'source' refers to any object in our catalogue, regardless of its classification; 'protostar' refers to an object in our catalogue identified either as a pre-main-sequence star or as containing an embedded protostellar source (those sources listed as 'P' or 'P?' in Table 1); and 'core' refers exclusively to those objects in our catalogue identified as starless cores ('C' or 'C?' in Table 1).

4.2 Source completeness

CuTEx detects sources through signal in the second derivatives of the original map. As a result, source detection is a function of both peak flux density and source FWHM, with sharply peaked sources being recovered better than extended sources with the same peak flux density. To test the completeness of our set of sources, we injected 50 identical Gaussian sources at random positions in the CO-subtracted SCUBA-2 850 μm map of L1688, and attempted to

Table 1. Results from multiple Gaussian fitting. Sources 1–70 are from the CO-subtracted section of L1688; 71–93 are from the remainder of L1688, L1689, L1709, and L1712. Position angles are measured east of north. FWHMs are as measured, without deconvolution. Sources are named following the conventions of MAN98/S08 for L1688, and NWA06 for L1689.

Source index	Full name JCMTLSG	Source name	RA 16°: (J2000)	Dec −24°: (J2000)	FWHM (arcsec)	Angle (°)	$F_{\nu(850\,\mu m)}^{peak}$ (Jy pixel^{-1})	$F_{\nu(850\,\mu m)}^{total}$ (Jy)	IR assn	Type	S08/ NWA06	Region
1	J162627.4-242352	SM1	26:27.36	23:52.8	20.4 × 16.2	178.7	0.651	6.762	S1	C	SM1	A
2	J162627.1-242334	SM1N	26:27.12	23:34.8	19.6 × 15.5	170.0	0.546	5.215	S1	C	SM1N	A
3	J162629.3-242425	SM2	26:29.28	24:25.2	29.0 × 17.2	139.0	0.279	4.389	S1	C	SM2	A
4	J162626.4-242428	VLA 1623	26:26.40	24:28.8	20.0 × 18.9	100.0	0.465	5.555	Y	P	VLA 1623	A
5	J162626.6-242233	A-MM5	26:26.64	22:33.6	36.2 × 18.0	106.2	0.074	1.519	S1	C?	A-MM5?	A
6	J162627.6-242302	A-MM6	26:27.60	23:02.4	30.9 × 22.1	169.6	0.209	4.474	S1	C	A-MM6	A
7	J162628.8-242233	A-MM7	26:28.80	22:33.6	28.3 × 19.2	24.3	0.113	1.929	S1	C?	A-MM7	A
8	J162631.4-242446	A-MM8	26:31.44	24:46.8	27.2 × 17.7	88.3	0.105	1.589	S1	C	A-MM8	A
9	J162621.8-242334	A-MM1	26:21.84	23:34.8	26.5 × 19.2	3.6	0.026	0.424	N?	C?	A-MM1?	A′
10	J162624.0-242150	A-MM4	26:24.00	21:50.4	27.2 × 17.7	88.3	0.035	0.525	N	C	A-MM4	A′
11	J162625.2-242136	A-MM4a	26:25.20	21:36.0	14.3 × 15.7	100.0	0.027	0.191	N	C	–	A′
12	J162645.1-242306	A-MM9	26:45.12	23:06.0	17.1 × 16.0	80.0	0.063	0.544	Y	P	A-MM9	A′
13	J162621.6-242247	A-MM10	26:21.60	22:48.0	17.8 × 19.1	174.9	0.085	0.911	Y	P?	A-MM10	A′
14	J162640.3-242710	A-MM15	26:40.32	27:10.8	17.3 × 15.8	79.5	0.028	0.241	Y	P	A-MM15	A′
15	J162643.4-241724	A-MM18	26:43.44	17:24.0	29.7 × 22.4	71.0	0.059	1.230	N	C	A-MM18	A′
16	J162624.0-241612	A-MM19	26:24.00	16:12.0	17.6 × 16.5	80.0	0.070	0.640	N	P	A-MM19	A′
17	J162610.3-242052	A-MM24	26:10.32	20:52.8	17.3 × 15.8	79.5	0.035	0.306	Y	P	A-MM24	A′
18	J162556.2-242045	A-MM25	25:56.16	20:45.6	17.3 × 15.8	99.5	0.016	0.139	Y	P	A-MM25	A′
19	J162610.1-241937	A-MM30	26:10.08	19:37.2	22.8 × 14.5	41.8	0.024	0.247	N	C	A-MM30	A′
20	J162630.5-242212	A-MM31	26:30.48	22:12.0	31.9 × 19.9	80.7	0.035	0.691	N?	C?	–	A′
21	J162624.0-242432	A-MM32	26:24.00	24:32.4	22.4 × 14.3	26.1	0.030	0.304	Y	P?	–	A′
22	J162617.3-242345	A-MM33	26:17.28	23:45.6	20.9 × 15.6	175.1	0.021	0.218	Y	P	–	A′
23	J162631.4-242157	A-MM34	26:31.44	21:57.6	30.0 × 20.6	90.9	0.038	0.736	S1	C?	–	A′
24	J162648.2-242837	A-MM35	26:48.24	28:37.2	17.3 × 15.8	99.5	0.007	0.065	Y	P	–	A′
25	J162710.3-241911	A-MM36	27:10.32	19:12.0	17.3 × 15.8	79.5	0.036	0.313	Y	P	–	A′
26	J162611.5-242443	A2-MM1	26:11.52	24:43.2	25.7 × 16.7	109.1	0.018	0.246	N	C	A2-MM1	A′
27	J162618.7-242508	A2-MM2	26:18.72	25:08.4	16.8 × 16.0	78.8	0.016	0.134	N	C	–	A′
28	J162610.1-242309	A3-MM1	26:10.08	23:09.6	29.4 × 20.1	94.9	0.025	0.474	N?	C?	A3-MM1	A′
29	J162712.2-242949	B1-MM3	27:12.24	29:49.2	26.9 × 19.2	136.6	0.048	0.779	N	C	B1-MM3	B1
30	J162715.1-243039	B1-MM4a	27:15.12	30:39.6	26.2 × 19.2	114.9	0.050	0.796	N	C	B1-MM4	B1
31	J162715.8-243021	B1-MM4b	27:15.84	30:21.6	19.5 × 12.9	38.4	0.021	0.165	N	C	–	B1
32	J162716.1-243108	B1-MM5	27:16.08	31:08.4	25.1 × 17.6	98.3	0.033	0.462	N	C	B1-MM5	B1
33	J162718.0-242851	B1B2-MM2	27:18.00	28:51.6	40.1 × 14.4	107.7	0.018	0.324	Y	P?	B1B2-MM2	B1B2
34	J162737.2-243032	B1B2-MM3	27:37.20	30:32.4	17.6 × 19.4	177.7	0.014	0.156	Y	P	–	B1B2
35	J162719.4-242714	B2-MM2a	27:19.44	27:14.4	27.1 × 18.2	26.8	0.028	0.441	N	C	B2-MM2	B2
36	J162720.6-242656	B2-MM2b	27:20.64	26:56.4	29.6 × 17.4	172.2	0.032	0.524	N	C	–	B2
37	J162724.2-242750	B2-MM4	27:24.24	27:50.4	14.3 × 15.7	80.0	0.052	0.365	N	C	B2-MM4	B2
38	J162725.7-242652	B2-MM6	27:25.68	26:52.8	32.6 × 18.0	156.2	0.077	1.412	N	C	B2-MM6	B2
39	J162727.6-242703	B2-MM8a	27:27.60	27:03.6	27.2 × 16.6	97.8	0.060	0.844	Y	P?	B2-MM8	B2
40	J162728.6-242703	B2-MM8b	27:28.56	27:03.6	39.1 × 17.7	152.6	0.043	0.929	Y	P?	B2-MM8	B2
41	J162729.5-242634	B2-MM9	27:29.52	26:34.8	34.5 × 20.6	150.1	0.072	1.607	N	C	B2-MM9	B2
42	J162729.5-242739	B2-MM10	27:29.52	27:39.6	33.2 × 18.0	141.6	0.084	1.571	Y	P	B2-MM10	B2
43	J162733.4-242616	B2-MM13	27:33.36	26:16.8	34.9 × 14.3	38.2	0.083	1.298	N	C	B2-MM13	B2
44	J162732.4-242634	B2-MM14	27:32.40	26:34.8	36.6 × 19.1	23.3	0.080	1.764	N	C	B2-MM14	B2
45	J162732.6-242703	B2-MM15	27:32.64	27:03.6	25.9 × 16.3	112.9	0.071	0.945	N	C	B2-MM15	B2
46	J162735.0-242616	B2-MM16	27:35.04	26:16.8	14.3 × 15.7	100.0	0.076	0.536	N	C	B2-MM16	B2
47	J162732.2-242735	B2-MM17	27:32.16	27:36.0	32.7 × 20.7	144.3	0.044	0.928	N	P?	–	B2
48	J162659.0-243426	C-MM3	26:59.04	34:26.4	28.8 × 19.5	117.0	0.041	0.718	N?	C	C-MM3	C
49	J162701.0-243440	C-MM6a	27:00.96	34:40.8	24.5 × 14.3	151.7	0.022	0.242	N?	C	C-MM6	C
50	J162702.2-243451	C-MM6b	27:02.16	34:51.6	28.3 × 19.2	48.3	0.018	0.311	N?	C	C-MM6	C
51	J162643.9-243447	C-MM11	26:43.92	34:48.0	17.8 × 19.1	74.9	0.025	0.271	Y	P?	C-MM11	C
52	J162708.9-243408	C-MM13	27:08.88	34:08.4	17.8 × 15.6	175.1	0.009	0.078	Y	P	–	C
53	J162704.8-243914	E-MM2d	27:04.80	39:14.4	28.1 × 15.8	148.4	0.037	0.522	N	C	E-MM2d	E
54	J162709.1-243719	E-MM6	27:09.12	37:19.2	23.2 × 19.2	155.7	0.035	0.489	Y	P?	E-MM6	E
55	J162705.0-243628	E-MM7	27:05.04	36:28.8	20.9 × 19.5	80.0	0.025	0.318	Y	P?	E-MM7	E
56	J162706.5-243813	E-MM9	27:06.48	38:13.2	17.6 × 16.7	80.0	0.020	0.185	Y	P?	E-MM9	E
57	J162715.4-243842	E-MM10	27:15.36	38:42.0	17.3 × 15.8	79.5	0.018	0.153	Y	P	E-MM10	E
58	J162721.6-243950	F-MM1	27:21.60	39:50.4	14.3 × 15.7	100.0	0.033	0.232	N	C	F-MM1	F
59	J162724.2-244102	F-MM2b	27:24.24	41:02.4	14.3 × 15.7	100.0	0.018	0.125	Y	P	F-MM2b	F
60	J162726.6-244048	F-MM3	27:26.64	40:48.0	17.1 × 19.5	100.0	0.047	0.498	Y	P	F-MM3	F
61	J162727.6-243928	F-MM4	27:27.60	39:28.8	19.8 × 19.1	175.1	0.030	0.360	Y	P	F-MM4	F

Table 1. – *continued*

Source index	Full name JCMTLSG	Source name	RA 16^h (J2000)	Dec −24^h (J2000)	FWHM (arcsec)	Angle (°)	$F_{\nu(850\,\mu m)}^{peak}$ (Jy pixel^{-1})	$F_{\nu(850\,\mu m)}^{total}$ (Jy)	IR assn	Type	S08/ NWA06	Region
62	J162739.4-243914	F-MM5	27:39.36	39:14.4	17.3 × 15.8	99.5	0.016	0.139	Y	P	F-MM5	F
63	J162711.0-244044	F-MM10	27:11.04	40:44.4	21.3 × 13.6	150.1	0.011	0.101	Y	P?	-	F
64	J162738.6-244019	F-MM11	27:38.64	40:19.2	17.6 × 15.9	80.0	0.009	0.080	Y	P	–	F
65	J162738.2-243657	F-MM12	27:38.16	36:57.6	17.6 × 15.9	171.5	0.008	0.072	Y	P	–	F
66	J162618.7-242819	J-MM1	26:18.72	28:19.2	17.6 × 15.9	80.0	0.023	0.207	Y	P	J-MM1	J
67	J162537.9-242233	J-MM7	25:37.92	22:33.6	17.3 × 15.8	99.5	0.021	0.178	Y	P	J-MM7	J
68	J162623.5-244311	J-MM8	26:23.52	43:12.0	17.3 × 15.8	86.4	0.051	0.444	Y	P	–	J
69	J162658.3-244536	J-MM9	26:58.32	45:36.0	17.6 × 15.5	93.6	0.049	0.422	Y	P	–	J
70	J162758.6-243339	H-MM1	27:58.56	33:39.6	29.2 × 18.5	38.6	0.050	0.845	N	C	–	88
71	J162816.3-243653	H-MM2	28:16.32	36:54.0	17.6 × 15.9	10.0	0.018	0.160	Y	P	-	88
72	J162821.4-243621	H-MM3	28:21.36	36:21.6	21.8 × 19.1	105.1	0.036	0.473	Y?	P?	–	88
73	J162845.1-242815	D/H-MM1	28:45.12	28:15.6	17.6 × 16.4	80.0	0.016	0.141	Y?	P	–	88
74	J162739.1-235819	88N SMM 1	27:39.12	58:19.2	19.4 × 13.3	32.8	0.008	0.066	Y?	?	–	88
75	J163157.1-245714	SMM 8	31:57.12	57:14.4	28.3 × 19.2	65.7	0.037	0.638	N	C	SMM 8	89S
76	J163201.0-245641	SMM 9	32:00.96	56:42.0	18.8 × 16.8	92.8	0.049	0.483	Y	P	SMM 9	89S
77	J163151.6-245620	SMM 11	31:51.60	56:20.4	28.9 × 19.2	82.8	0.029	0.517	Y	P	SMM 11	89S
78	J163153.5-245558	SMM 12	31:53.52	55:58.8	22.8 × 14.5	158.2	0.036	0.378	N?	C	SMM 12	89S
79	J163200.2-245544	SMM 13	32:00.24	55:44.4	14.3 × 15.7	86.2	0.025	0.179	N	C	SMM 13	89S
80	J163137.7-244947	SMM 16a	31:37.68	49:48.0	29.2 × 18.5	161.4	0.021	0.363	N	C	SMM 16	89S
81	J163138.9-244958	SMM 16b	31:38.88	49:58.8	14.3 × 15.7	80.0	0.019	0.137	N	C	SMM 16	89S
82	J163142.0-244933	SMM 16c	31:42.00	49:33.6	28.1 × 16.1	109.9	0.026	0.365	N	C	SMM 16	89S
83	J163355.7-244203	SMM 17	33:55.68	42:03.6	17.8 × 16.3	15.1	0.017	0.152	Y	P	SMM 17	89E
84	J163228.8-242909	SMM 19	32:28.80	29:09.6	14.3 × 15.7	80.0	0.154	1.093	N?	C?	SMM 19	89N
85	J163222.6-242833	SMM 20	32:22.56	28:33.6	21.2 × 19.0	79.5	1.489	18.846	Y?	P	SMM 20	89N
86	J163230.0-242847	SMM 22	32:30.00	28:48.0	23.5 × 14.3	44.7	0.058	0.611	N?	C	–	89N
87	J163226.6-242811	SMM 23	32:26.64	28:12.0	25.6 × 21.4	23.6	0.003	0.046	N	C	–	89N
88	J163221.6-242739	SMM 24	32:21.60	27:39.6	22.1 × 18.8	74.3	0.023	0.295	N?	C	–	89N
89	J163133.4-242735	SMM 25	31:33.36	27:36.0	17.6 × 16.1	80.0	0.018	0.161	Y?	P	–	89N
90	J163131.2-242624	SMM 26	31:31.20	26:24.0	17.6 × 15.5	80.0	0.013	0.110	Y?	P	–	89N
91	J163135.5-240126	1709 SMM 1	31:35.52	1:26.4	21.0 × 15.9	82.6	0.073	0.772	Y?	P	–	09
92	J163143.4-240017	1709 SMM 2	31:43.44	0:18.0	18.1 × 16.8	93.5	0.023	0.217	N?	C	–	09
93	J163945.4-240202	1712 SMM 1	39:45.36	2:02.4	17.6 × 17.4	80.0	0.037	0.353	–	P	–	12

recover these with CuTEx. We repeated this process for various source sizes and peak flux densities. For each source size and peak flux density, we repeated the source injection and recovery process 10 times, and took the completeness fraction to be the mean fraction of sources recovered.

For our mean non-deconvolved source FWHM of 19.7 arcsec, CuTEx recovered 50 per cent of injected sources with a peak flux density of 0.011 Jy 6 arcsec pixel^{-1}, and 80 per cent with a peak flux density of 0.020 Jy 6 arcsec pixel^{-1}. At our mean source temperature of ∼13.5 K, these peak flux densities are equivalent to masses of 0.040 M$_\odot$ (50 per cent) and 0.051 M$_\odot$ (80 per cent). (See Section 4.3 for a discussion of determination of temperatures and derivation of masses.) The 80 per cent completeness limit at 13.5 K as a function of deconvolved source FWHM is shown as a solid line on Fig. 5, below.

The completeness limit in crowded regions of emission will be slightly higher and less certain than the completeness limit in sparsely populated regions, as in crowded regions tightly-packed or superimposed sources must be separated. In regions of the SCUBA-2 850 μm map where $F_\nu > 10\sigma$, we found a 50 per cent mass completeness limit of 0.047 ± 0.005 M$_\odot$ at 13.5 K, approximately consistent with, but slightly more uncertain than, the completeness limit across the map as a whole. We note that completeness is likely to vary somewhat across the map, and that the completeness limits given in the paragraph above and shown on Fig. 5 are average values.

4.3 Source characterization from continuum data

Table 3 lists the properties of our set of sources derived from SCUBA-2 and *Herschel* continuum data. The deconvolved FWHMs of the sources were determined using the SCUBA-2 850-μm equivalent beam size of 14.1 arcsec (Dempsey et al. 2013). The equivalent radius of each source was calculated as the geometric mean of the two deconvolved FWHMs.

The data at 160, 450 and 850 μm were convolved to the 250 μm resolution of 18 arcsec using the convolution kernels described above. Flux densities were measured from the spatially filtered *Herschel* 160 and 250 μm data and the two sets of SCUBA-2 data using elliptical apertures with major and minor axis diameters of twice the measured (i.e. non-deconvolved) major and minor FWHMs of each of the sources (enclosing 99.5 per cent of the total flux density in a Gaussian distribution). The resulting SED of each source was fitted with a modified blackbody distribution, in order to determine the mean line of sight dust temperature of our sources. The monochromatic flux density F_ν is given at frequency ν by

$$\lambda F_\lambda = \nu F_\nu = \nu \Omega f B_\nu(T) \left(1 - e^{-\left(\frac{\nu}{\nu_c}\right)^\beta} \right), \qquad (9)$$

where $B_\nu(T)$ is the Planck function at dust temperature T, Ω is the solid angle of the aperture, f is the filling factor of the source in the aperture, $\nu_c = 6$ THz is the frequency at which the optical

Table 2. Protostellar sources in Ophiuchus, with alternate identifications and classes, where known. EESG09 – Enoch et al. (2009); WGA08 – Wilking, Gagné & Allen (2008); AM94 – André & Montmerle (1994); DoAr – Dolidze & Arakelyan (1959); VSSG – Vrba et al. (1975); WL – Wilking & Lada (1983); YLW – Young, Lada & Wilking (1986), LFAM – Leous et al. (1991); GY – Greene & Young (1992); GWAYL – Greene et al. (1994); ISO-Oph – Bontemps et al. (2001); EESG09 Oph-emb – Enoch et al. (2009); EDJ2009 – Evans et al. (2009). Note that in WGA08 classifications, Arabic numerals indicate a class determined from an IRAC SED while Roman numerals indicate a class determined from a 3.6–24 µm spectral index. F indicates a flat spectrum.

Source index	Source ID	Alternate ID	Class	Class reference
4	VLA 1623	EESG09 Oph-emb 3	0	EESG09
12	A-MM9	GY 116, VSSG 28, ISO-Oph 67	2,II	WGA08
13	A-MM10	LFAM 1, ISO-Oph 31	F,–	WGA08
14	A-MM15	GY 91, ISO-Oph 54, EESG09 Oph-emb 22	I	EESG09
16	A-MM19	YLW 32 ISO-Oph 40	II	AM94
17	A-MM24	ISO-Oph 17	2,II	WGA08
18	A-MM25	DoAr 20, YLW 25, ISO-Oph 6	II	AM94
21	A-MM32	GY 21, LFAM 3, ISO-Oph 37	F,F	WGA08
22	A-MM33	ISO-Oph 21	1,I	WGA08
24	A-MM35	GY 128, ISO-Oph 7, EESG09 Oph-emb 23	I	EESG09
25	A-MM36	SR 21(A?), YLW 8(A?), ISO-Oph 110	2,–	WGA08
33	B1B2-MM2	YLW 12A/B?, ISO-Oph 124/125?, EESG09 Oph-emb 11	I	EESG09
34	B1B2-MM3	YLW 46, GY 304, ISO-Oph 159	2,–	WGA08
39	B2-MM8a	GPJ2008 8		
40	B2-MM8b	YEE2006 20		
42	B2-MM10	GY 279, ISO-Oph 147, EESG09 Oph-emb 26	I	EESG09
47	B2-MM17	WLY 1-17?		
51	C-MM11	WL 12, YLW 2, ISO-Oph 65	1,–	WGA08
52	C-MM13	WL10, GY 211, ISO-Oph 105	2,II	WGA08
54	E-MM6	WL 15, ISO-Oph 108, EESG09 Oph-emb 16	I	EESG09
55	E-MM7	GY 197, ISO-Oph 99, EESG09 Oph-emb 6	1,I	WGA08
56	E-MM9	GY 205, ISO-Oph 103, EESG09 Oph-emb 12	I	EESG09
57	E-MM10	WL 20W/E?, GY 240A/B? ISO-Oph 121	–,–/2,–	WGA08
59	F-MM2b	GY 263, EESG09 Oph-emb 12	I	EESG09
60	F-MM3	GY 265, ISO-Oph 141, EESG09 Oph-emb 14	I	EESG09
61	F-MM4	GY 269, ISO-Oph 143, EESG09 Oph-emb 13	I	EESG09
62	F-MM5	GY 314, ISO-Oph 166	2,F	WGA08
63	F-MM10	GY 224, ISO-Oph 112	F,F	WGA08
64	F-MM11	GY 312, ISO-Oph 165	1,I	WGA08
65	F-MM12	YLW 47, GY 308, ISO-Oph 163	2,II	WGA08
66	J-MM1	YLW31, VSSG 1, ISO-Oph 24	F,II	WGA08
67	J-MM7	ISO-Oph 2		
68	J-MM8	DoAr 25, YLW 34, ISO-Oph 38	II	AM94
69	J-MM9	DoAr 29, ISO-Oph 88	II	AM94
71	H-MM2	YLW 58, ISO-Oph 196	II	AM94
72	H-MM3	EDJ2009 954, EESG09 Oph-emb 1	0	EESG09
73	D/H-MM1	DoAr40	II	AM94
74	88N SMM 1	DoAr 33	II?	AM94
76	SMM 9	GWAYL 6, ISO-Oph 209, EESG09 Oph-emb 10	I	EESG09
77	SMM 11	GWAYL 5?, ISO-Oph 204? LDN 1689 IRS 5?		
83	SMM 17	EDJ2009 1013		
85	SMM 20	IRAS 16293−2422B, EESG09 Oph-emb 2	0	EESG09
89	SMM 25	DoAr 44	II	AM94
90	SMM 26	EDG2009 984		
91	1709 SMM 1	GWAYL 4, EDJ2009 989, EESG09 Oph-emb 17	I	EESG09
93	1712 SMM 1	IRAS 16367−2356, EDJ2009 989		

depth is taken to become unity (Ward-Thompson, André & Kirk 2002), and β is the dust emissivity index, here taken to be 2.0. Fig. 4 shows three example SEDs. This process allows determination of the average temperature of the material within the aperture. There will be some line-of-sight confusion between cold dust associated with the source (which will itself not be isothermal) and warmer foreground and background emission, possibly leading to an overestimation of source temperatures. However, the spatial filtering introduced by the SCUBA-2 data reduction process should reduce the contamination by extended emission. In crowded regions in which sources overlap significantly, the measured flux densities may be contaminated by emission from neighbouring sources. We emphasize that the temperatures reported here are line-of-sight averages.

Table 3. Properties derived from SCUBA-2 and Herschel data (see text for discussion).

Source index	Source ID	Temperature (K)	850 μm mass ($M_\odot$)	Column density ($\times 10^{22}$ cm^{-2})	Density ($\times 10^6$ cm^{-3})
1	SM1	17.2 ± 0.6	1.298 ± 0.134	30.520 ± 3.161	9.609 ± 0.995
2	SM1N	17.3 ± 0.6	0.999 ± 0.104	29.477 ± 3.077	10.398 ± 1.085
3	SM2	18.5 ± 0.7	0.758 ± 0.082	7.758 ± 0.837	1.612 ± 0.174
4	VLA 1623	16.4 ± 0.5	1.158 ± 0.117	19.788 ± 2.006	5.311 ± 0.538
5	A-MM5	18.6 ± 0.7	0.259 ± 0.028	1.761 ± 0.192	0.298 ± 0.032
6	A-MM6	18.8 ± 0.8	0.752 ± 0.083	4.810 ± 0.529	0.790 ± 0.087
7	A-MM7	21.7 ± 1.0	0.262 ± 0.031	2.348 ± 0.278	0.456 ± 0.054
8	A-MM8	18.4 ± 0.7	0.276 ± 0.030	3.003 ± 0.322	0.643 ± 0.069
9	A-MM1	16.6 ± 0.6	0.087 ± 0.010	0.860 ± 0.096	0.176 ± 0.020
10	A-MM4	16.3 ± 0.5	0.110 ± 0.011	1.194 ± 0.125	0.256 ± 0.027
11	A-MM4a	15.9 ± 0.5	0.042 ± 0.005	4.918 ± 0.555	3.468 ± 0.392
12	A-MM9	10.2 ± 0.2	0.268 ± 0.025	11.071 ± 1.053	4.621 ± 0.440
13	A-MM10	19.5 ± 0.9	0.144 ± 0.017	3.137 ± 0.360	0.950 ± 0.109
14	A-MM15	13.6 ± 0.4	0.069 ± 0.008	2.812 ± 0.311	1.167 ± 0.129
15	A-MM18	14.8 ± 0.4	0.301 ± 0.029	1.988 ± 0.194	0.332 ± 0.032
16	A-MM19	9.3 ± 0.3	0.382 ± 0.042	12.759 ± 1.399	4.788 ± 0.525
17	A-MM24	15.5 ± 0.5	0.070 ± 0.008	2.858 ± 0.309	1.186 ± 0.128
18	A-MM25	16.2 ± 0.6	0.030 ± 0.004	1.206 ± 0.172	0.501 ± 0.071
19	A-MM30	16.0 ± 0.5	0.053 ± 0.006	1.245 ± 0.139	0.391 ± 0.044
20	A-MM31	22.9 ± 1.2	0.087 ± 0.011	0.616 ± 0.077	0.106 ± 0.013
21	A-MM32	15.5 ± 0.5	0.069 ± 0.008	1.740 ± 0.197	0.568 ± 0.064
22	A-MM33	16.0 ± 0.5	0.047 ± 0.006	1.144 ± 0.134	0.365 ± 0.043
23	A-MM34	22.8 ± 1.2	0.093 ± 0.012	0.680 ± 0.085	0.119 ± 0.015
24	A-MM35	10.0 ± 0.2	0.033 ± 0.006	1.368 ± 0.238	0.568 ± 0.099
25	A-MM36	14.7 ± 0.5	0.078 ± 0.009	3.188 ± 0.366	1.324 ± 0.152
26	A2-MM1	15.8 ± 0.5	0.054 ± 0.006	0.724 ± 0.085	0.172 ± 0.020
27	A2-MM2	15.0 ± 0.4	0.032 ± 0.004	1.429 ± 0.183	0.618 ± 0.079
28	A3-MM1	17.6 ± 0.7	0.088 ± 0.010	0.687 ± 0.077	0.125 ± 0.014
29	B1-MM3	12.2 ± 0.3	0.270 ± 0.025	2.618 ± 0.240	0.529 ± 0.049
30	B1-MM4a	11.8 ± 0.2	0.293 ± 0.026	2.972 ± 0.267	0.614 ± 0.055
31	B1-MM4b	11.9 ± 0.3	0.059 ± 0.006	3.431 ± 0.375	1.695 ± 0.185
32	B1-MM5	12.1 ± 0.3	0.163 ± 0.015	2.066 ± 0.193	0.477 ± 0.045
33	B1B2-MM2	15.8 ± 0.5	0.071 ± 0.008	0.580 ± 0.066	0.107 ± 0.012
34	B1B2-MM3	16.4 ± 0.8	0.032 ± 0.005	0.693 ± 0.107	0.208 ± 0.032
35	B2-MM2a	11.4 ± 0.2	0.172 ± 0.016	1.795 ± 0.169	0.376 ± 0.035
36	B2-MM2b	11.6 ± 0.2	0.199 ± 0.019	1.941 ± 0.180	0.393 ± 0.037
37	B2-MM4	11.8 ± 0.3	0.134 ± 0.013	15.826 ± 1.481	11.162 ± 1.045
38	B2-MM6	11.3 ± 0.2	0.562 ± 0.050	4.477 ± 0.399	0.820 ± 0.073
39	B2-MM8a	13.5 ± 0.4	0.243 ± 0.024	2.975 ± 0.289	0.676 ± 0.066
40	B2-MM8b	13.8 ± 0.4	0.258 ± 0.025	1.613 ± 0.159	0.262 ± 0.026
41	B2-MM9	11.6 ± 0.3	0.606 ± 0.055	3.651 ± 0.334	0.582 ± 0.053
42	B2-MM10	15.8 ± 0.5	0.345 ± 0.035	2.676 ± 0.268	0.484 ± 0.049
43	B2-MM13	10.3 ± 0.2	0.623 ± 0.053	6.408 ± 0.546	1.334 ± 0.114
44	B2-MM14	10.7 ± 0.2	0.791 ± 0.068	4.875 ± 0.421	0.786 ± 0.068
45	B2-MM15	11.8 ± 0.3	0.346 ± 0.031	4.763 ± 0.431	1.147 ± 0.104
46	B2-MM16	10.4 ± 0.2	0.252 ± 0.022	29.785 ± 2.584	21.008 ± 1.823
47	B2-MM17	13.4 ± 0.3	0.272 ± 0.026	1.756 ± 0.168	0.290 ± 0.028
48	C-MM3	12.3 ± 0.3	0.244 ± 0.025	2.083 ± 0.210	0.395 ± 0.040
49	C-MM6a	12.8 ± 0.4	0.077 ± 0.009	1.564 ± 0.179	0.457 ± 0.052
50	C-MM6b	13.2 ± 0.4	0.094 ± 0.011	0.837 ± 0.095	0.163 ± 0.018
51	C-MM11	13.5 ± 0.4	0.078 ± 0.008	1.694 ± 0.180	0.513 ± 0.054
52	C-MM13	15.0 ± 0.5	0.019 ± 0.003	0.720 ± 0.129	0.291 ± 0.052
53	E-MM2d	13.6 ± 0.4	0.149 ± 0.015	1.879 ± 0.187	0.433 ± 0.043
54	E-MM6	20.1 ± 0.9	0.074 ± 0.009	0.933 ± 0.111	0.215 ± 0.025
55	E-MM7	16.1 ± 0.6	0.068 ± 0.008	0.999 ± 0.113	0.249 ± 0.028
56	E-MM9	15.0 ± 0.5	0.045 ± 0.005	1.433 ± 0.173	0.528 ± 0.064
57	E-MM10	16.3 ± 0.6	0.032 ± 0.004	1.306 ± 0.172	0.542 ± 0.071
58	F-MM1	15.3 ± 0.5	0.054 ± 0.006	6.381 ± 0.691	4.501 ± 0.488
59	F-MM2b	15.6 ± 0.5	0.028 ± 0.004	3.307 ± 0.427	2.333 ± 0.301
60	F-MM3	16.7 ± 0.6	0.101 ± 0.011	2.294 ± 0.246	0.711 ± 0.076
61	F-MM4	20.0 ± 0.9	0.055 ± 0.007	0.952 ± 0.114	0.257 ± 0.031
62	F-MM5	11.1 ± 0.3	0.057 ± 0.008	2.344 ± 0.321	0.973 ± 0.133
63	F-MM10	12.9 ± 0.3	0.031 ± 0.005	1.066 ± 0.155	0.403 ± 0.059

Table 3. – *continued*

Source index	Source ID	Temperature (K)	850 μm mass ($M_\odot$)	Column density ($\times 10^{22}$ cm^{-2})	Density ($\times 10^6$ cm^{-3})
64	F-MM11	8.7 ± 0.2	0.055 ± 0.010	2.093 ± 0.367	0.836 ± 0.146
65	F-MM12	13.5 ± 0.4	0.021 ± 0.004	0.788 ± 0.147	0.315 ± 0.059
66	J-MM1	8.3 ± 0.2	0.161 ± 0.020	6.099 ± 0.756	2.435 ± 0.302
67	J-MM7	8.9 ± 0.3	0.116 ± 0.015	4.741 ± 0.628	1.968 ± 0.261
68	J-MM8	10.3 ± 0.3	0.212 ± 0.022	8.656 ± 0.911	3.593 ± 0.378
69	J-MM9	11.8 ± 0.3	0.155 ± 0.017	6.519 ± 0.700	2.747 ± 0.295
70	H-MM1	11.0 ± 0.2	0.358 ± 0.031	3.214 ± 0.282	0.626 ± 0.055
71	H-MM2	11.5 ± 0.3	0.062 ± 0.007	2.340 ± 0.282	0.934 ± 0.113
72	H-MM3	12.5 ± 0.3	0.156 ± 0.015	2.216 ± 0.213	0.542 ± 0.052
73	D/H-MM1	10.5 ± 0.3	0.065 ± 0.009	2.234 ± 0.296	0.850 ± 0.113
74	88N SMM 1	8.2 ± 0.3	0.053 ± 0.011	2.800 ± 0.605	1.322 ± 0.286
75	SMM 8	11.3 ± 0.2	0.253 ± 0.023	2.263 ± 0.207	0.440 ± 0.040
76	SMM 9	19.0 ± 0.8	0.080 ± 0.009	2.125 ± 0.245	0.712 ± 0.082
77	SMM 11	14.6 ± 0.4	0.131 ± 0.013	1.126 ± 0.114	0.215 ± 0.022
78	SMM 12	14.3 ± 0.4	0.098 ± 0.010	2.292 ± 0.230	0.720 ± 0.072
79	SMM 13	12.8 ± 0.3	0.056 ± 0.006	6.654 ± 0.712	4.693 ± 0.502
80	SMM 16a	12.3 ± 0.3	0.124 ± 0.013	1.116 ± 0.112	0.217 ± 0.022
81	SMM 16b	12.5 ± 0.3	0.045 ± 0.005	5.341 ± 0.624	3.767 ± 0.440
82	SMM 16c	11.7 ± 0.3	0.136 ± 0.013	1.664 ± 0.162	0.377 ± 0.037
83	SMM 17	10.5 ± 0.3	0.070 ± 0.009	2.357 ± 0.295	0.886 ± 0.111
84	SMM 19	11.8 ± 0.3	0.402 ± 0.036	47.367 ± 4.264	33.409 ± 3.007
85	SMM 20	17.4 ± 0.7	3.555 ± 0.393	53.954 ± 5.961	13.649 ± 1.508
86	SMM 22	11.5 ± 0.3	0.235 ± 0.022	5.274 ± 0.485	1.624 ± 0.149
87	SMM 23	12.8 ± 0.3	0.015 ± 0.005	0.128 ± 0.040	0.025 ± 0.008
88	SMM 24	13.6 ± 0.4	0.084 ± 0.009	1.200 ± 0.130	0.295 ± 0.032
89	SMM 25	9.6 ± 0.2	0.090 ± 0.011	3.253 ± 0.406	1.269 ± 0.158
90	SMM 26	11.0 ± 0.3	0.046 ± 0.007	1.950 ± 0.293	0.820 ± 0.123
91	1709 SMM 1	12.9 ± 0.4	0.240 ± 0.025	5.436 ± 0.573	1.681 ± 0.177
92	1709 SMM 2	11.0 ± 0.2	0.092 ± 0.009	2.684 ± 0.275	0.942 ± 0.096
93	1712 SMM 1	5.8 ± 0.1	0.716 ± 0.089	20.386 ± 2.534	7.064 ± 0.878
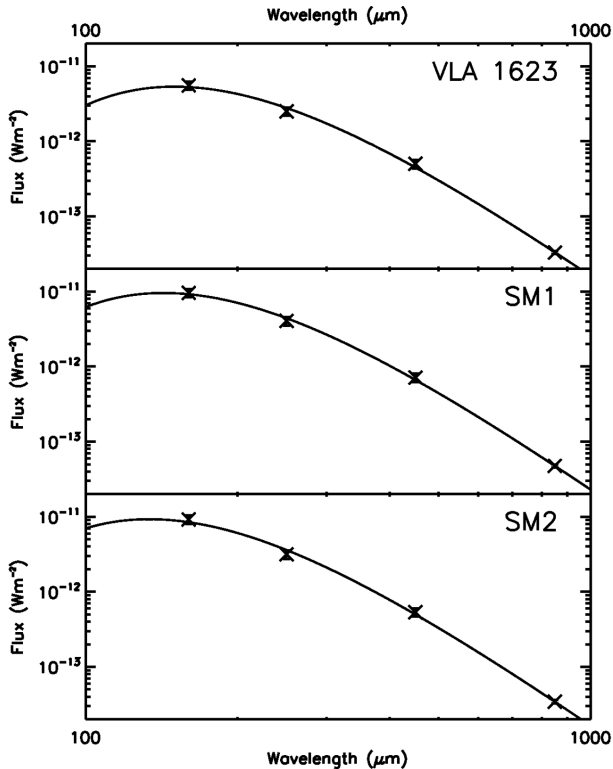
Figure 4. Example SED fits for sources VLA1623, SM1, and SM2.

Masses were calculated from the best-fitting model 850-μm flux densities and dust temperatures of our sources following the Hildebrand ([1983]) formulation

$$M = \frac{F_{\nu(850\,\mu\text{m})}D^2}{\kappa_{\nu(850\,\mu\text{m})}B_{\nu(850\,\mu\text{m})}(T)}, \quad (10)$$

where $F_{\nu(850\,\mu\text{m})}$ is the modelled total flux density at 850 μm, D is the distance to Ophiuchus (139 ± 6 pc; Mamajek [2008]), $B_{\nu(850\,\mu\text{m})}(T)$ is the Planck function, and $\kappa_{\nu(850\,\mu\text{m})}$ is the dust opacity, as parametrized by Beckwith et al. ([1990]): $\kappa_\nu = 0.1(\nu/10^{12}\,\text{Hz})^\beta$ cm^2 g^{-1} (assuming a standard dust-to-gas ratio of 1:100). Again, the dust emissivity index β was taken to be 2.0.

For the protostellar sources in our catalogue, the temperatures, and hence the masses, determined from the dust emission are those of the protostellar envelope, and not of the protostar itself. The modified blackbody model used to fit temperatures is applicable only to envelope-dominated sources; the temperatures and masses determined for the Class II protostars in our catalogue (listed in Table 2) may not be representative.

The mean volume density for each source was calculated assuming that the third axis of each source is the geometric mean of its major and minor axes. Then, number density n is calculated as

$$n = \frac{M}{\mu m_{\text{H}}} \frac{1}{\frac{4}{3}\pi R^3}, \quad (11)$$

where R is the equivalent deconvolved radius, as defined above. Similarly, the column density N of each source is calculated as

$$N = \frac{M}{\mu m_{\mathrm{H}}} \frac{1}{\pi R^2}, \qquad (12)$$

and in both cases, the mean molecular weight μ is taken to be 2.86, assuming that the gas is $\sim$70 per cent H_2 by mass (Kirk et al. 2013).

One of our sources, SMM 23, located in the centre of L1689N, has a very low best-fitting peak flux density, 0.003 Jy 6 arcsec pixel^{-1}. This is due to SMM 23 being located between SMM 20/IRAS 16293−2422 and SMM 19, the brightest and second-brightest sources in L1689N, respectively, leading to the majority of flux at SMM 23's position being assigned to the two nearby bright sources in the fitting process. We consider SMM 23 to be robustly detected by CuTEx, and so determine its temperature and mass. However, due to its properties being poorly constrained by the fitting process, we exclude SMM 23 from all subsequent analysis, leaving 46 starless cores for further analysis.

4.4 Source mass distribution

Fig. 5 shows the distribution of mass with size for the starless cores (those objects marked 'C' and 'C?' in Table 1) in our sample, compared with previous studies of the same region: MAN98 (with their masses and radii scaled to account for their assumption of a distance of 160 pc) and S08. Our cores are comparable in size to those found in previous studies. The masses of the cores in our sample are comparable to those found by MAN98, while the masses found by S08 are typically higher.

The grey band shown in Fig. 5 indicates the behaviour expected for transient, gravitationally unbound CO clumps (Elmegreen & Falgarone 1996). Gravitationally bound prestellar cores are expected to occupy the upper part of the mass/size diagram (Motte et al. 2001), being overdense compared to transient, unbound structure.

Before *Herschel*, there was discussion of whether starless and prestellar cores are two different populations, separated in the mass/size plane (see e.g. Ward-Thompson et al. 2007, and references therein). More recent studies have found cores occupying intermediate locations in the mass/size plane (Könyves et al. 2010; Kirk et al. 2013), indicating that prestellar and unbound starless cores are all part of the same population. Our cores are restricted to the 'prestellar' region in which previous studies have found the starless cores in L1688 to lie (MAN98; S08). The limit on our ability to recover faint sources is the CuTEx completeness limit. The 80 per cent completeness limit, as a function of source size (at a temperature of 13.5 K) is shown as a solid line on Fig. 5. However, the 5σ sensitivity limit of the SCUBA-2 850 μm data (again for a temperature of 13.5 K), shown as a dashed line on Fig. 5, is such that regardless of our choice of source extraction algorithm, we are not sensitive to material occupying the 'unbound' regions of the mass/size plane.

Fig. 6 shows the mass distribution of our cores. The mass distribution is consistent with the lognormal + power-law distribution expected for core mass functions (CMFs – Chabrier 2003), and previously seen in Ophiuchus by MAN98 and S08. We fitted a function of the form $N \propto M^{-\gamma}$ to the mass distribution, and found that, for bins centred on masses greater than or equal to 0.2 $M_\odot$, the best-fitting power-law index was $\gamma = 1.0 \pm 0.4$, equivalent to a CMF power-law index of $\alpha = \gamma + 1 = 2.0 \pm 0.4$.

The traditional method of determining the power-law index of the CMF by fitting to binned data is liable to lead to a loss of accuracy in the fitted model. We attempted to ameliorate this issue by also analysing the cumulative distribution function of core masses using the maximum likelihood (ML) estimator for an infinite power-law distribution (Koen 2006; Maschberger & Kroupa 2009), calculated over the same mass range ($M \geq 0.2 M_\odot$). The cumulative distribution and fits are shown in Fig. 7. The empirical cumulative distribution function $\hat{F}$ is given, for the ith data point in our sample, by
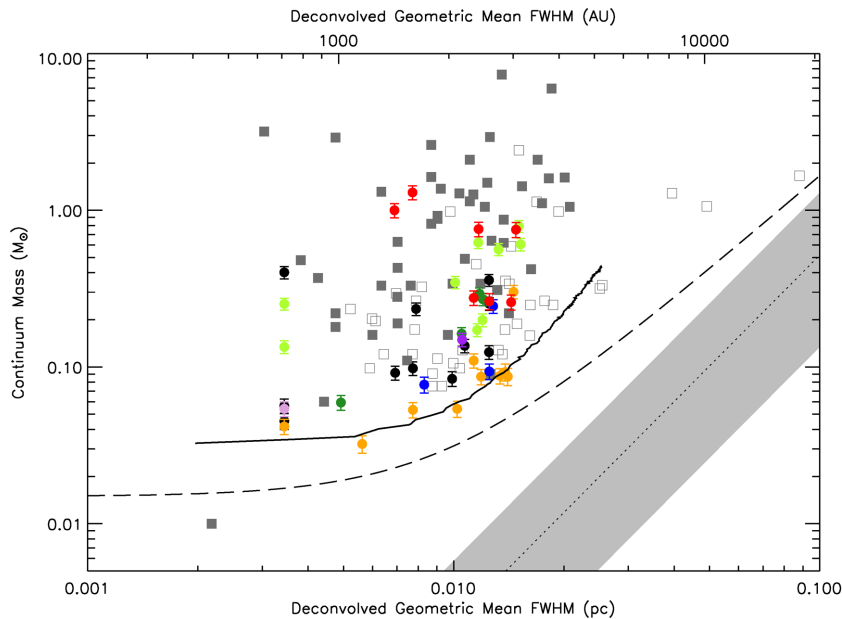

Figure 5. Comparison of the masses of our starless cores, calculated from the continuum data, with their deconvolved radii. Circles with error bars: this study. Open squares: MAN98. Filled squares: S08. Grey band: $M_{\mathrm{CO}} \propto R_{\mathrm{CO}}^{2.35}$ relation (Elmegreen & Falgarone 1996). Solid line: 80 per cent completeness limit. Dashed line: 5σ sensitivity limit. Both limits assume a temperature of 13.5 K. Red symbols are cores in Oph A; orange, Oph A$'$; dark green, Oph B1; light green, Oph B2; blue, Oph C; dark purple, Oph E; light purple, Oph F; black, elsewhere in the cloud.
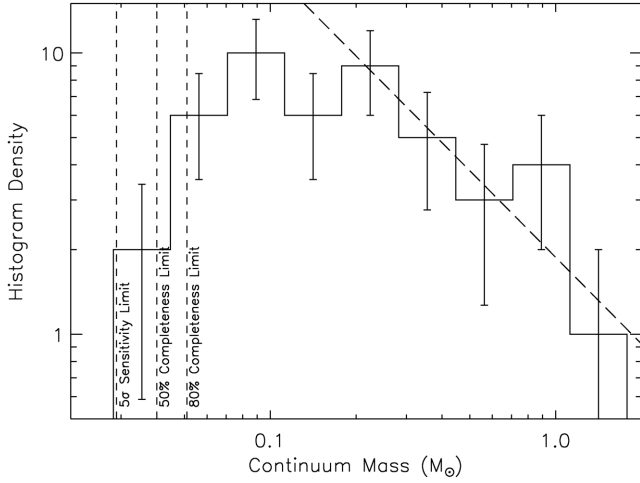
Figure 6. Core mass distribution, with best-fitting power-law index $\alpha = 2.0 \pm 0.4$ for cores with masses $>0.2\,\mathrm{M_\odot}$ plotted as a dashed line. The 5σ sensitivity limit and 50 per cent completeness limits for a temperature of 13.5 K are also shown.
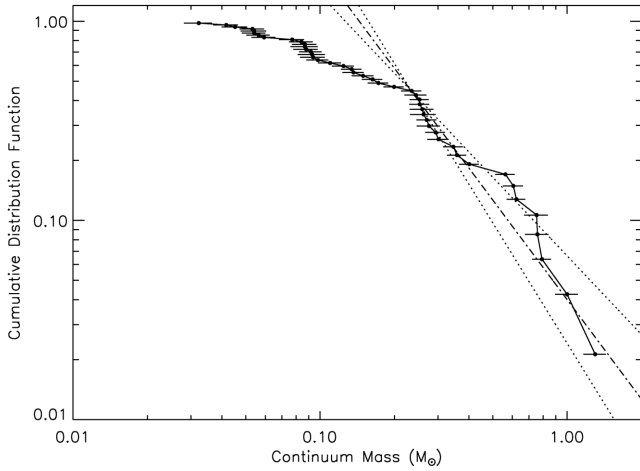

Figure 7. Cumulative mass distribution function, with UML estimator power-law index $\alpha_{\mathrm{uml}} = 2.7$ for cores with masses $>0.2\,\mathrm{M_\odot}$ plotted as a dot–dashed line, and its $1\sigma \pm 0.4$ error limits plotted as dotted lines.

$$\hat{F}(X_i) \equiv \frac{i}{n+1}, \tag{13}$$

where n is the number of data points X. The ML estimator for the exponent α of an infinite power-law distribution is

$$\alpha_{\mathrm{ml}} = 1 + \frac{n}{\left(\sum_{i=1}^{n} X_i\right) - n \ln\left(\min(X)\right)}. \tag{14}$$

The unbiased maximum likelihood (UML) estimator, α_{uml} is then

$$\alpha_{\mathrm{uml}} = 1 + \frac{n-1}{n}(\alpha_{\mathrm{ml}} - 1). \tag{15}$$

The CMF power-law index found by this method was $\alpha_{\mathrm{uml}} = 2.7 \pm 0.4$. Uncertainties were estimated by performing a set of Monte Carlo experiments, drawing a set of data points randomly from our distribution of masses, from which α_{ml} was recalculated. The error quoted is the standard deviation of the distribution of α_{uml} which results from this procedure.

In both cases, the power-law index is consistent with the high-mass power-law tail of the initial mass function (IMF), $\alpha = 2.3$ (Salpeter 1955; Kroupa 2001). That our two estimators for the

power-law index only marginally agree with one another is likely a result of low number statistics.

Previous studies of the starless core population of Ophiuchus have found similar slopes for the high-mass distribution of core masses. MAN98 found a slope of $\alpha \sim 1.5$ in the mass range 0.1–0.5 $\mathrm{M_\odot}$ and $\alpha \sim 2.5$ in the mass range 0.5–3.0 $\mathrm{M_\odot}$. Johnstone et al. (2000) found a similar behaviour: $\alpha = 1.5$ for $M \leq 0.6\,\mathrm{M_\odot}$ and $\alpha = 2.0$–2.5 for $M > 0.6\,\mathrm{M_\odot}$. Sadavoy et al. (2010) found a power-law slope of $\alpha = 2.26 \pm 0.20$ in the mass range 0.3 $\mathrm{M_\odot} < M < 5\,\mathrm{M_\odot}$. Our mass functions are consistent with the high-mass behaviour found by MAN98 and Johnstone et al. (2000), and with Sadavoy et al. (2010) at all masses considered.

We conclude that our CMF is consistent with having a high-mass slope similar to that of the IMF, and with the CMFs found by previous studies of the same region. The similarity between the CMF and IMF has been noted in many recent studies of molecular clouds (e.g. Nutter & Ward-Thompson 2007), leading to suggestions that the form of the IMF is caused by cloud fragmentation prior to the prestellar core stage of star formation (see e.g. André et al. 2014, and references therein).

4.5 Source characterization from spectral data

The typical column densities, masses, and velocity dispersions derived from N_2H^+ and $C^{18}O$ data were estimated for each core for which data were available. For each core, the velocity dispersion was taken to be the average of the velocity dispersions in each good pixel covered by the aperture used for source photometry, while the mass was taken to be the average of the masses in the good pixels in the aperture, multiplied by the total number of pixels in the aperture. The starless core properties derived from N_2H^+ and $C^{18}O$ data are listed in Table 5.

Of the emission from the three isotopologues of CO mapped by HARP, that of $C^{18}O$ was chosen as it has the lowest optical depth, typically <0.5, but reaching ~ 2 in high-density regions (White et al. 2015). $C^{18}O$ emission can only probe the outer envelopes of starless cores; the freeze-out of heavy molecules on to dust grains at high densities and low temperatures means that CO (or its isotopologues) cannot be considered a reliable tracer for densities $n(H_2) > 10^5\,\mathrm{cm^{-3}}$ (see e.g. Di Francesco et al. 2007, and references therein). Although Ophiuchus is known to have low average levels of CO depletion (Christie et al. 2012), $C^{18}O$ linewidths can only be used as a conservative measure of the bound state of a core, providing information on the behaviour of the moderately dense cloud material.

N_2H^+ emission is a better tracer of the bound state of the densest parts of starless cores than $C^{18}O$, with significant depletion not occurring until core densities exceed $\sim 10^6\,\mathrm{cm^{-3}}$ (Di Francesco et al. 2007, and references therein). However, due to the low abundance of N_2H^+ relative to H_2 ($X(N_2H^+) = 5.2 \pm 0.5 \times 10^{-10}$; Pirogov et al. 2003), it is only detectable in regions of the highest H_2 column density.

Each pixel was fitted using an IDL routine utilizing *mpfit* (Markwardt 2009). For $C^{18}O$, a single Gaussian was fitted to each pixel, and fits with SNR ≥ 5 were accepted. For N_2H^+, a seven-component set of Gaussians were fitted to the multiplet, and fits were accepted for pixels where the weakest component had SNR ≥ 2.

Column densities, and hence masses, were calculated for each core, using the CO and N_2H^+ data sets. Column densities were calculated following Garden et al. (1991):

$$N = \frac{3k_\mathrm{B}}{8\pi^3 B \mu_D^2} \frac{e^{hBJ(J+1)/k_\mathrm{B}T_\mathrm{ex}}}{J+1} \frac{T_\mathrm{ex} + \frac{hB}{3k_\mathrm{B}}}{1 - e^{-h\nu/k_\mathrm{B}T_\mathrm{ex}}} \int \tau \, \mathrm{d}\upsilon, \tag{16}$$

where N is the column density of the species in question, B and μ_D are the rotational constant and permanent dipole moment of the molecule respectively, and J is the lower rotational level of the transition. The excitation temperature, T_{ex}, can be calculated as follows (see e.g. Pineda, Caselli & Goodman 2008)

$$T_{ex} = \frac{T_0}{\ln\left(1 + T_0\left(\frac{T_R}{1-e^{-\tau}} + \frac{T_0}{e^{T_0/T_{bg}}-1}\right)^{-1}\right)}, \tag{17}$$

where $T_0 = h\nu/k_B$, T_{bg} is the cosmic microwave background temperature, 2.73 K, and T_R is the radiation temperature of the spectral line.

The integral in equation (16) can be written as (see e.g. Buckle et al. 2010):

$$\int \tau(v)dv = \frac{1}{J(T_{ex}) - J(T_{bg})} \int \frac{\tau(v)}{1-e^{-\tau(v)}} T_{MB}dv \tag{18}$$

$$\approx \frac{1}{J(T_{ex}) - J(T_{bg})} \frac{\tau(v_0)}{1-e^{-\tau(v_0)}} \int T_{MB}dv, \tag{19}$$

where v_0 is the central velocity of the line, T_{MB} is the observed main beam temperature and $J(T)$ is the source function,

$$J(T) = \frac{T_0}{e^{T_0/T} - 1} \tag{20}$$

with T_0 defined as above.

Excitation temperatures and optical depths for $C^{18}O$ were calculated under the assumption that the ^{13}CO and $C^{18}O$ emission trace material with the same excitation temperature, and that ^{13}CO is optically thick everywhere. The excitation temperature is calculated using equation (17) in the limit $\tau_{13CO} \gg 1$, with $T_R = T_{max,^{13}CO}$. The optical depth of $C^{18}O$ is determined using the relation

$$\frac{T_{max,C^{18}O}}{T_{max,^{13}CO}} = \frac{1-e^{-\tau_{C^{18}O}}}{1-e^{-\tau_{13CO}}}, \tag{21}$$

and the abundance ratio $[^{13}CO/C^{18}O]=5.5$ (Frerking, Langer & Wilson 1982), i.e. $\tau_{13CO} = 5.5\tau_{C^{18}O}$.

For $C^{18}O$, B and μ_D were taken from the NIST data base (Johnson 2013): $B = 5.79384 \times 10^{10}$ s^{-1}, and $\mu_D = 0.112$ D. Thus, equation (16) becomes

$$N(C^{18}O) = 7.94 \times 10^8 e^{16.88/T_{ex}} \frac{T_{ex} + 0.927}{1-e^{-16.88/T_{ex}}}$$
$$\times \frac{1}{J(T_{ex}) - J(2.73\,K)} \frac{\tau}{1-e^{-\tau}} \Delta v \sum_i T_i \text{ cm}^{-2}, \tag{22}$$

where Δv is the velocity channel width in cm s^{-1}, and T_i is the best-fitting main beam temperature in the ith velocity channel. The equivalent H_2 column density is found using the conversion factor $X(C^{18}O) = 2.635 \times 10^{-7}$. This value of $X(C^{18}O)$ was determined from the relations $N(H_2)/A_V = 9.4 \times 10^{20}$ cm^2 mag^{-1} (Pineda et al. 2010, and references therein), and $N(^{12}CO)/A_V = 1.01 \times 10^{17}$ cm^2 mag^{-1} (Pineda et al. 2010), i.e. $N(H_2)/N(^{12}CO) = 1.1 \times 10^4$. For the abundance ratios $[^{13}CO/C^{18}O]=5.5$ (Frerking et al. 1982) and $[^{12}CO/^{13}CO]=69$ (Wilson 1999), this leads to the value of $X(C^{18}O)$ given above. The accuracy of the H_2 column densities calculated using this abundance ratio depends on all of the above relations being valid in Ophiuchus and consistent across all of our cores. The total uncertainty resulting from all of these relations is difficult to quantify, but we state conservatively that our column densities determined from $C^{18}O$ emission are likely to be accurate to within a factor of a few.

The hyperfine splitting of the N_2H^+ multiplet allows for the direct calculation of optical depth. The optical depths of any pair of hyperfine transitions $j \to i$ and $m \to l$ are related to one another by their hyperfine statistical weights and Einstein A coefficients (see e.g. Emerson 1999, p. 308):

$$\frac{\tau_{ji}}{\tau_{ml}} = \frac{g_j A_{ji}}{g_m A_{ml}}. \tag{23}$$

Neglecting any background contribution, the relative strengths of the two lines will be

$$\frac{T_{max,ji}}{T_{max,ml}} = \frac{T_{ex,ji}}{T_{ex,ml}} \frac{1-e^{-\tau_{ji}}}{1-e^{-\tau_{ml}}}. \tag{24}$$

Assuming that the excitation temperature is the same for all of the hyperfine transitions, the relative strengths of each of the hyperfine components can be expressed as a function of optical depth, and hence optical depth can be fitted as a free parameter. The excitation temperature can then be calculated using equation (17). For each of the 15 hyperfine components, equation (16) becomes

$$N_i = 3.10 \times 10^6 \frac{T_{ex} + 0.745}{1 - e^{-h\nu_i/k_B T_{ex}}}$$
$$\times \frac{1}{J(T_{ex}) - J(2.73\,K)} \frac{\tau_i}{1-e^{-\tau_i}} \Delta v \sum_j T_j \text{ cm}^{-2}, \tag{25}$$

where T_j is the best-fitting model main beam temperature of the of the ith hyperfine component in the jth velocity channel. The frequencies and Einstein A coefficients of the hyperfine transitions are taken from Daniel, Cernicharo & Dubernet (2006), while the parameters $B = 4.65869 \times 10^{10}$ s^{-1} and $\mu_D = 3.40$ D are taken from the CDMS data base (Müller et al. 2001). Summing over all hyperfine components, the total N_2H^+ column density is

$$N(N_2H^+) = \sum_{i=1}^{15} N_i. \tag{26}$$

The equivalent H_2 column density is found using the conversion factor $X(N_2H^+) = 5.2 \times 10^{-10}$ (Pirogov et al. 2003). We note that Pirogov et al. (2003) determined this value of $X(N_2H^+)$ by considering the mean N_2H^+ abundance across 36 massive molecular cloud cores; the applicability of this abundance to a low-to-intermediate-mass star-forming region such as Ophiuchus is not certain. Friesen et al. (2010) find N_2H^+ abundances in the range 2.5–17×10^{-10} in Oph B, while Di Francesco et al. (2004) find a mean N_2H^+ abundance of 1.3×10^{-10} in Oph A, indicating N_2H^+ depletion in the Oph A region. These results suggest that the Pirogov et al. (2003) value of $X(N_2H^+)$ is applicable to our cores, but that a wide scatter about this abundance is to be expected, and hence our H_2 column densities determined using this abundance are likely to be accurate to within a factor of 2–3 in regions without significant N_2H^+ depletion.

Fig. 8 compares the masses derived from each of our tracers, and shows that the masses of cores measured in N_2H^+ and in continuum emission correlate fairly well, although with significant scatter about the line of unity, whereas those from $C^{18}O$ do not. This correlation indicates that N_2H^+ and dust are tracing the same material. The excess in continuum mass over N_2H^+ mass in the most massive cores in Oph A indicates that N_2H^+ is not tracing the very innermost regions of the densest cores. As discussed above, depletion of N_2H^+ in the densest regions of Oph A has been previously noted by Di Francesco et al. (2004). There is also considerable variation in core mass from region to region, as shown by the coloured symbols. We return to a discussion of this variation in Section 6.
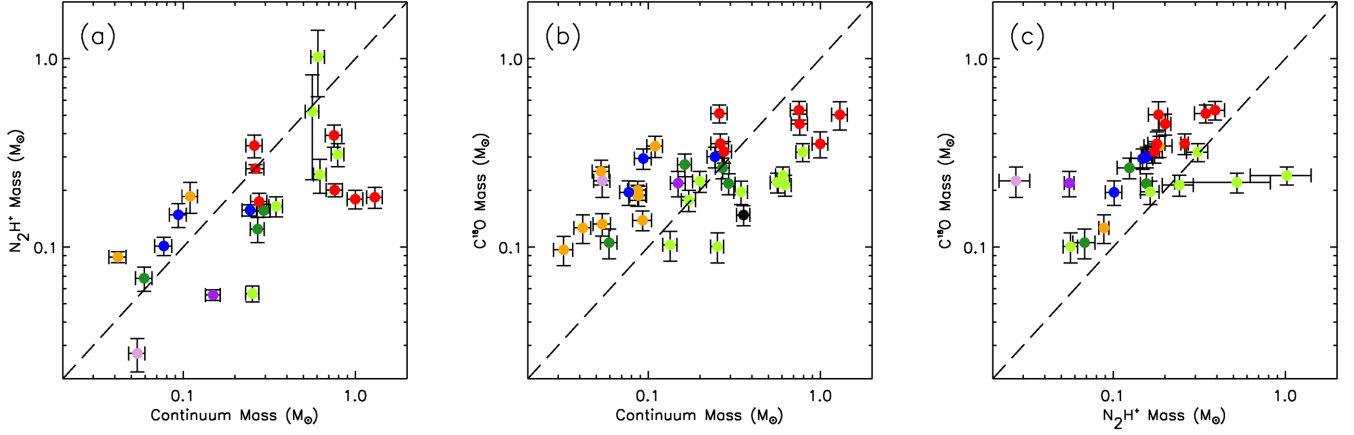
Figure 8. Comparison of masses calculated from continuum, N_2H^+ and $C^{18}O$ emission. Panel (a) compares continuum- and N_2H^+-derived masses, for the 23 cores for which N_2H^+ data are available. Panel (b) compares continuum- and $C^{18}O$-derived masses, for the 35 cores for which $C^{18}O$ data are available. Panel (c) compares N_2H^+- and $C^{18}O$-derived masses, for the 23 N_2H^+ cores. Colour coding is as in Fig. 5. The dashed line is the line of unity.

It should be noted that different subsets of our set of starless cores are shown in each panel of Fig. 8. $C^{18}O$ data are available at the positions of 35 of the 46 starless cores which we are analysing (as shown in Fig. 8 b). N_2H^+ data are available for 23 of these 35 cores (shown in Fig. 8 a). There are no cores for which N_2H^+ data are available and $C^{18}O$ data are not (i.e. the samples shown in Figs 8(a) and (c) are identical, and are a subset of those in Fig. 8 b). The $C^{18}O$ and N_2H^+ masses of all cores for which data are available are listed in Table 5. The virial analysis in Section 5 is performed only on those 23 cores for which continuum, $C^{18}O$ and N_2H^+ data are all available.

5 ENERGY BALANCE AND STABILITY

We estimate the magnitude of each of the terms in the virial equation in order to determine the energy balance, and hence the stability against collapse, of the cores in our sample. We consider the virial equation in the form

$$\frac{1}{2}\ddot{\mathcal{I}} = 2\Omega_K + \Omega_G + \Omega_M + \Omega_P, \tag{27}$$

where $\ddot{\mathcal{I}}$ is the second derivative of the moment of inertia, Ω_K is the internal energy, Ω_G is the gravitational potential energy, Ω_M is the magnetic energy, and Ω_P is the energy due to external pressure acting on the core. If $\ddot{\mathcal{I}} < 0$, a core's net energy is negative, and hence the core is collapsing. Conversely, a core with $\ddot{\mathcal{I}} > 0$ will be dispersing, and the virially stable mass of a core is the mass at which $\ddot{\mathcal{I}} = 0$.

5.1 Gravitational and internal energy

The first two terms on the right-hand side of equation (27) can be estimated from directly measured quantities. The internal kinetic energy of a core of mass M and one-dimensional (1D) velocity dispersion σ is given by the relation

$$\Omega_K = \frac{3}{2}M\sigma^2, \tag{28}$$

where σ is the velocity dispersion for the mean gas particle, related to the velocity dispersion in the tracer molecule ($\sigma_{N_2H^+}$) by

$$\sigma^2 = \sigma_{N_2H^+}^2 + k_B T_{gas}\left(\frac{1}{\mu m_H} - \frac{1}{m_{N_2H^+}}\right), \tag{29}$$
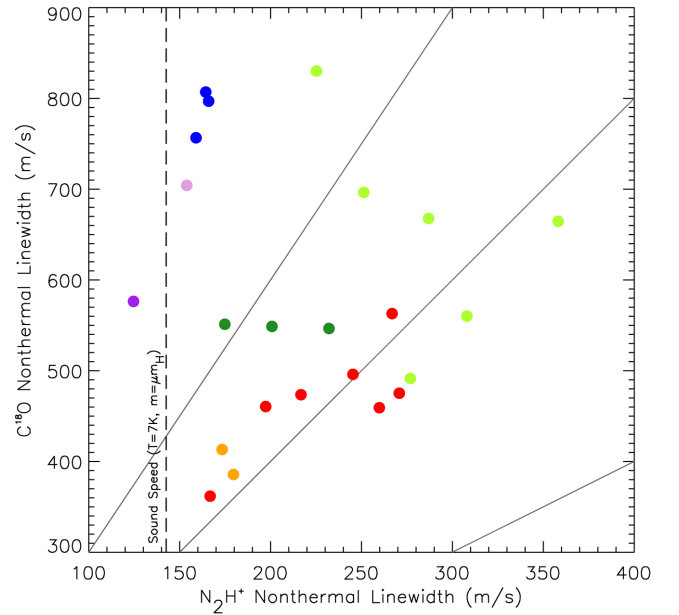

Figure 9. Comparison of mean non-thermal linewidths for the 23 cores for which N_2H^+ data are available, as measured in $C^{18}O$ and N_2H^+. The dashed line shows the mean gas sound speed at a temperature of 7 K. Grey lines show the 1:1, 2:1 and 3:1 $C^{18}O$:N_2H^+ linewidth ratios. Colour coding is as in Fig. 5.

where T_{gas} is the typical gas temperature of the material traced by N_2H^+ (see Fuller & Myers 1992). We assume that N_2H^+ traces material at $T_{gas} \approx 7$ K (Stamatellos, Whitworth & Ward-Thompson 2007). We apply a similar correction to the $C^{18}O$ linewidths, there taking T_{gas} to be the mean line-of-sight temperature of the core. However, as discussed below, $C^{18}O$ linewidths are significantly supersonic, making the effect of this correction minimal.

The non-thermal component of the linewidth, σ_{NT}, can be derived using the gas temperature T_{gas}, and the relation $\sigma^2 = \sigma_T^2 + \sigma_{NT}^2$, where the sound speed, σ_T, is given by $\sqrt{k_B T_{gas}/m}$, and m is the mass of the molecule being considered ($m_{C^{18}O} = 30$ atomic mass units (amu); $m_{N_2H^+} = 29$ amu). Fig. 9 compares the non-thermal N_2H^+ and $C^{18}O$ linewidths of our cores, with the sound speed in gas at 7 K marked as a vertical line.

All of our cores have supersonic non-thermal velocity dispersions in $C^{18}O$. The non-thermal velocity dispersions in N_2H^+ are consistently smaller than those measured in $C^{18}O$, typically being transonic or mildly supersonic. This indicates a loss of turbulence between the material traced by $C^{18}O$ and the denser material traced by N_2H^+. Transitions from supersonic turbulence at low densities to coherence at high densities have been observed in dense cores both in molecular clouds (e.g. Goodman et al. 1998; Caselli et al. 2002; Pineda et al. 2010) and in isolation (Quinn 2013). This behaviour is consistent with models of turbulent dissipation (e.g. Klessen et al. 2005; Offner, Klein & McKee 2008). The ratio between the non-thermal velocity dispersion in $C^{18}O$ and the non-thermal velocity dispersion in N_2H^+ varies from region to region: in Oph B, $\sigma_{NT}(C^{18}O)/\sigma_{NT}(N_2H^+) \sim 2.5$ while in Oph C, the ratio is ~ 5, suggesting that turbulence has been dissipated more in Oph C than in Oph B.

In keeping with the model used to characterize our sources, the gravitational potential energy is that of a spherically symmetric Gaussian density distribution, $\rho(r) = \rho_0 e^{-r^2/2\alpha^2}$ ($\alpha = $ FWHM/$\sqrt{8\ln 2}$):

$$\Omega_G = -\frac{1}{2\sqrt{\pi}} \frac{GM^2}{\alpha} \tag{30}$$

(see Appendix C for a derivation). We take α to be the geometric mean of the deconvolved Gaussian widths of each of our cores.

For our mean core mass, $0.27\,M_\odot$, and deconvolved size, FWHM $= 0.01$ pc, the gravitational potential energy $|\langle\Omega_G\rangle| \approx 4 \times 10^{41}$ erg, and for our mean 1D N_2H^+ velocity dispersion, 225 ms^{-1} (equivalent to $\sigma = 262$ m s^{-1}), the kinetic energy term in the virial equation is $2\langle\Omega_K\rangle \approx 11 \times 10^{41}$ erg. Hence, these two terms are of similar order to one another, with the kinetic term slightly dominant.

5.2 External gas pressure

Previous studies of starless cores in Ophiuchus have suggested that external gas pressure might be instrumental in confining dense cores. Maruta et al. (2010) estimate a typical surface pressure on cores in Ophiuchus of $\langle P_{EXT}\rangle/k_B \approx 3 \times 10^6$ K cm^{-2}, sufficient to influence the energy balance of the cores. Similarly, Johnstone et al. (2000) estimate core surface pressures $P_{EXT}/k_B \sim 10^{6-7}$ K cm^{-3} by treating the starless cores they identify in Ophiuchus as pressure-confined Bonnor–Ebert (BE) spheres.

We consider the gas pressure in material traced by $C^{18}O$ to be the external pressure acting on our starless cores, since CO becomes significantly depleted through freeze-out on to dust grains at densities $\gtrsim 10^5$ cm^{-3} (Di Francesco et al. 2007), and as such is expected to trace the outer layers, or envelopes, of starless cores. Higher-density tracers such as N_2H^+ are expected to trace the denser inner material of the cores themselves.

The external pressure term in the virial equation, Ω_P, is given by

$$\Omega_P = -3P_{EXT}V = -4\pi P_{EXT}R^3 \tag{31}$$

for a core of volume V being acted on by an external pressure P_{EXT}. P_{EXT} can be estimated from the ideal gas law:

$$P_{EXT} \approx \rho_{c^{18}O}\langle\sigma^2_{gas,c^{18}O}\rangle, \tag{32}$$

where $\rho_{c^{18}O}$ is the density at which the transition between $C^{18}O$ and N_2H^+ being effective tracers occurs, and $\langle\sigma^2_{gas,c^{18}O}\rangle$ is the mean gas velocity dispersion in material traced by $C^{18}O$. We assume that $C^{18}O$ does not trace densities higher than 10^5 cm^{-3}. We must

estimate a radius at which core density drops to 10^5 cm^{-3} in order to determine the volume over which this surface pressure acts. We continue to assume that our cores are characterized by Gaussian density distributions, in which case the radius at which the density drops to $\rho_{c^{18}O}$ is given by

$$r_{c^{18}O} = \alpha\sqrt{2\ln\left(\frac{\rho_0}{\rho_{c^{18}O}}\right)}. \tag{33}$$

The peak core density ρ_0 can be estimated from the measured mean density $\langle\rho_{FWHM}\rangle$ of each core (listed in Table 3), which is determined over an area of radius $1 \times$FWHM:

$$\rho_0 = \frac{\langle\rho_{FWHM}\rangle}{3}(8\ln 2)^{3/2}\left(\sqrt{\frac{\pi}{2}}\,\text{erf}\left(2\sqrt{\ln 2}\right) - \frac{\sqrt{2\ln 2}}{8}\right)^{-1}. \tag{34}$$

These equations give typical $r_{c^{18}O}$ values in the range ~ 0.7–1.5 FWHM.

The mean energy due to external gas pressure on the material traced by N_2H^+ estimated from this method is 9×10^{41} erg, roughly the same order of magnitude as the mean internal kinetic energy of our cores. This is equivalent to $\langle P_{EXT}\rangle/k_B \approx 1.8 \times 10^7$ K cm^{-3}, an order of magnitude higher pressure than that found by Maruta et al. (2010), but similar to the total pressure in Ophiuchus $P/k_B \sim 2 \times 10^7$ K cm^{-3} estimated by Johnstone et al. (2000).

5.3 External pressure from ionizing photons

In Ophiuchus, the effects of the B2V star HD 147889 dominate the effects of the interstellar radiation field (Stamatellos et al. 2007). According to the cloud geometry model of Liseau et al. (1999), Oph A is the region of the cloud closest to HD 147889, at a distance of 1.1 pc. Furthermore, the B3–B5 star S1 appears to be influencing Oph A. We estimate the pressure on cores in Oph A from ionizing photons from these B stars, as being indicative of the maximum external pressure acting on any of the cores in our sample.

The pressure term of the virial equation due to ionizing photons from an early-type star irradiating one side of a starless core is given by Ward-Thompson et al. (2006) as

$$\Omega_P \approx 2\pi R^3 P_{ext} \sim \frac{4R^2 k_B T_{II}}{D}\left(\frac{3\pi\dot{N}_{LyC}R}{\alpha_*}\right)^{1/2}, \tag{35}$$

where R is the radius of the core; D is the distance from the core to the exciting star; $T_{II} \sim 10^4$ K is the canonical temperature for gas in an H II region; $\alpha_* \approx 2 \times 10^{-13}$ cm^3 s^{-1} is the recombination coefficient for atomic hydrogen into excited states at T_{II} and $\dot{N}_{LyC}$ is the rate at which Lyman continuum photons are emitted from the exciting star.

We take the number of Lyman continuum photons emitted per unit surface area of the star, $\dot{N}^0_{LyC}$, from Dottori (1980), assuming in both cases $\log g \sim 4.25$ (Strom & Peterson 1968). The total rate of ionizing photons is then $\dot{N}_{LyC} = 4\pi R^2_{star}\dot{N}^0_{LyC}$, where the stellar radii are listed in Table 4. We take the distance to HD 147889 to be 1.1 pc, and the distance to S1 to be 0.06 pc, the plane-of-sky distance

Table 4. Adopted B star properties.

Star	Luminosity (L$_\odot$)	T_{eff} (K)	Radius (R$_\odot$)	$\log_{10}(\dot{N}^0_{LyC})$ (cm^{-2}s^{-1})
HD 147889	4700	22 300	4.6	20.4
S1	1500	17 200	4.4	18.5

between the star S1 and the core SM1 at our assumed distance to Ophiuchus. For a core radius equal to our mean deconvolved core FWHM, 0.01 pc, the external pressure terms for a core in Oph A in close proximity to S1 will be

$$\Omega_{\text{P,HD}} \sim 3.4 \times 10^{40} \text{ erg} \tag{36}$$

$$\Omega_{\text{P,S1}} \sim 6.6 \times 10^{40} \text{ erg}. \tag{37}$$

Hence, the maximum value we expect the ionizing photon pressure term to take anywhere in Oph A is $\Omega_{\text{P}} \lesssim 10^{41}$ erg, and outside Oph A, where the effect of HD 147889 will be lessened, and the effect of S1 will be minimal, we expect $\Omega_{\text{P}} \sim 10^{40}$ erg. Hence, we conclude that ionizing photon pressure represents a small correction to the virial balance of our cores, typically being one to two orders of magnitude smaller than the gravitational and kinetic energy terms, and that we are justified in neglecting it in our virial analysis.

5.4 Magnetic energy density

Neither the strength nor the relative importance of magnetic fields in Ophiuchus are well known. There have to date been only a few reliable measurements of magnetic fields in the cloud (Crutcher et al. 1993; Goodman & Heiles 1994; Troland et al. 1996). The magnetic field at intermediate densities, measured through Zeeman splitting in OH (Crutcher et al. 1993; Troland et al. 1996), is what we consider in the subsequent analysis, as more representative of the magnetic field in the molecular gas. Troland et al. (1996) find the line-of-sight magnetic field strength $|B_{\text{los}}|$ to be 10 μG at a density of $10^{3.2}$ cm^{-3}, and find a 1D velocity dispersion in OH of ~ 0.57 km s^{-1}.

The magnetic field strength in the turbulent ISM is commonly related to the non-thermal velocity dispersion and density of the ISM (see e.g. Basu 2000, and references therein):

$$B = B_0 \frac{\sigma_{\text{NT}}}{\sigma_{\text{NT,0}}} \left(\frac{n}{n_0} \right)^{1/2}, \tag{38}$$

where the subscript '0' indicates the reference (measured) value of each quantity. We note that this relation implies a constant ratio between turbulent and magnetic energy. The magnetic energy can be expressed as

$$\Omega_{\text{M}} = \frac{B^2 V}{2\mu_0} = \frac{1}{2\mu_0} \left(\frac{B_0^2}{\rho_0 \sigma_{0,\text{NT}}^2} \right) M \sigma_{\text{NT}}^2, \tag{39}$$

while the non-thermal component of the kinetic energy, $\Omega_{\text{K, NT}}$, is given by $1.5 M \sigma_{\text{NT}}^2$ (see equation 28). Thus, the ratio between turbulent and magnetic energy is given by

$$\frac{\Omega_{\text{M}}}{\Omega_{\text{K,NT}}} = \frac{1}{3\mu_0} \frac{B_0^2}{\rho_0 \sigma_{0,\text{NT}}^2}, \tag{40}$$

which, for the values of B_0, ρ_0, and $\sigma_{0, \text{NT}}$ given by Crutcher et al. (1993) and Troland et al. (1996), gives a ratio of $\Omega_{\text{M}}/\Omega_{\text{K, NT}} = 0.11$ for the Ophiuchus molecular cloud. Therefore, for our cores (if equation 38 holds) the magnetic energy of a core cannot exceed ~ 10 per cent of the core's internal energy. In the case of transonic or subsonic motions within the core, the fraction will be smaller still. Furthermore, the internal energy term in the virial equation is $2\Omega_{\text{K}}$, while the magnetic energy term is merely Ω_{M}. Consequently, the contribution of magnetic energy to core stability will in this case be ~ 5 per cent that of the turbulent kinetic energy. Therefore, we also neglect the magnetic energy term in our virial analysis. We

note the need for further measurements of magnetic field strengths in high-density regions, in order to test the validity of analyses of this kind.

5.5 Core stability

On average, for those cores in our sample for which N$_2$H$^+$ and C^{18}O data are available, the gravitational potential energy and the external pressure energy are of similar magnitude, and together slightly dominate over the internal energy. However, there is a wide variation from core to core. Table 5 lists the values of gravitational potential energy, internal energy, external pressure energy, and the virial parameter for all those cores for which data are available.

Fig. 10 shows the ratio of Ω_{G} to Ω_{P} plotted against $-(\Omega_{\text{G}} + \Omega_{\text{P}})/2\Omega_{\text{K}}$, the virial stability criterion. The vertical dashed line marks the locus of virial stability. It can be seen that the majority of our cores lie to the right of this line, indicating that they are virially bound. Of the 23 cores for which N$_2$H$^+$ data are available, 22 are either bound or virialized, having a virial ratio $-(\Omega_{\text{G}} + \Omega_{\text{P}})/2\Omega_{\text{K}} \geq 1$. However, as can be seen in Fig. 10, one core, in Oph A$'$, is marginally unbound, with virial ratio < 1, and with uncertainty on this ratio such that a ratio of 1 is consistent.

The horizontal dashed line on Fig. 10 marks the division between those cores that are gravitationally bound (above the line) and those that are pressure-confined (below the line). There is a wide variation from region to region, with Oph A being the most gravitationally bound and Oph C being the most highly pressure-confined. These differences are discussed further in Section 6. It should be noted that a full virial analysis has only been performed on those cores located in regions targeted for N$_2$H$^+$ observations, i.e. the regions of highest column density. The results of this analysis cannot necessarily be generalized to the cores for which N$_2$H$^+$ data are not available.

5.6 BE critical mass

The BE model of a starless core (Bonnor 1956; Ebert 1955) is frequently used as a measure of the stability of starless cores (e.g. Alves, Lada & Lada 2001). The BE model treats a core as an isothermal, self-gravitating, polytropic sphere bounded by external pressure. The mass at which a BE sphere at temperature T, with sound speed $c_s(T)$, and bounded by external pressure P_{EXT}, is critically stable against gravitational collapse is given by

$$M_{\text{BE,crit}} = 1.18 \frac{c_s(T)^4}{P_{\text{EXT}}^{1/2} G^{3/2}}. \tag{41}$$

The critical BE mass is often considered a useful proxy for virial mass as, if the critically-stable BE model is appropriate and the radius at which cores are bounded by external pressure can be estimated, the stability of a core can be estimated without velocity dispersion data, as cores with observed masses greater than their critically-stable BE mass (i.e. $M/M_{\text{BE,crit}} > 1$) will be undergoing gravitational collapse.

We investigated whether the critical BE stability criterion ($M/M_{\text{BE,crit}}$) can accurately predict the virial balance of starless cores in L1688, and hence whether it can be reliably used as a proxy for virial mass in regions for which line data are not available. We determined the critically stable masses of our cores by considering the external pressure, P_{EXT}, on our cores to be the gas pressure in C^{18}O. The critically stable BE masses and continuum masses of the subset of our cores for which N$_2$H$^+$ data are available are compared in Fig. 11. Critically stable BE masses for the remainder of the set of cores for which C^{18}O data are available are listed

Table 5. Properties of starless cores, derived from spectral line data and from virial arguments and the BE criterion.

Source index	Source name	N_2H^+ mass $(M_\odot)$	$C^{18}O$ mass $(M_\odot)$	Bonnor–Ebert mass $(M_\odot)$	$-\Omega_G$ $(\times 10^{41}$ erg)	Ω_K $(\times 10^{41}$ erg)	$-\Omega_P$ $(\times 10^{41}$ erg)	$\frac{1}{2}\ddot{\mathcal{I}}$ $(\times 10^{41}$ erg)
1	SM1	0.184 ± 0.023	0.503 ± 0.086	0.261 ± 0.196	124.2	36.3	5.9	-57.4
2	SM1N	0.179 ± 0.020	0.353 ± 0.056	0.221 ± 0.168	82.4	27.3	5.9	-33.7
3	SM2	0.201 ± 0.016	0.450 ± 0.057	0.308 ± 0.244	27.9	13.4	11.3	-12.4
5	A-MM5	0.345 ± 0.048	0.511 ± 0.056	0.305 ± 0.242	2.7	5.2	10.1	-2.3
6	A-MM6	0.391 ± 0.053	0.532 ± 0.061	0.297 ± 0.239	21.7	18.1	19.9	-5.5
7	A-MM7	0.260 ± 0.013	0.354 ± 0.045	0.425 ± 0.374	3.1	6.9	8.0	$+2.6$
8	A-MM8	0.174 ± 0.019	0.321 ± 0.042	0.387 ± 0.303	3.8	4.0	4.4	-0.3
9	A-MM1	–	0.188 ± 0.024	0.180 ± 0.136	0.4	–	7.2	–
10	A-MM4	0.186 ± 0.035	0.343 ± 0.045	0.288 ± 0.207	0.6	1.7	3.0	-0.2
11	A-MM4a	0.088 ± 0.006	0.126 ± 0.022	0.255 ± 0.179	0.3	0.6	0.3	$+0.7$
19	A-MM30	–	0.251 ± 0.038	0.151 ± 0.107	0.2	–	4.2	–
20	A-MM31	–	0.200 ± 0.023	0.580 ± 0.530	0.3	–	2.7	–
23	A-MM34	–	0.138 ± 0.017	0.624 ± 0.569	0.4	–	2.5	–
26	A2-MM1	–	0.132 ± 0.018	0.202 ± 0.145	0.2	–	3.0	–
27	A2-MM2	–	0.097 ± 0.017	0.143 ± 0.098	0.1	–	1.7	–
28	A3-MM1	–	0.187 ± 0.023	0.220 ± 0.169	0.3	–	6.6	–
29	B1-MM3	0.124 ± 0.019	0.263 ± 0.033	0.113 ± 0.067	3.5	4.1	10.8	-6.1
30	B1-MM4a	0.156 ± 0.012	0.217 ± 0.028	0.107 ± 0.062	4.2	6.5	10.7	-1.9
31	B1-MM4b	0.068 ± 0.010	0.105 ± 0.019	0.109 ± 0.064	0.4	1.1	1.2	$+0.5$
32	B1-MM5	–	0.274 ± 0.038	0.121 ± 0.071	1.4	–	5.8	–
35	B2-MM2a	–	0.177 ± 0.023	0.116 ± 0.066	1.5	–	6.0	–
36	B2-MM2b	–	0.223 ± 0.028	0.092 ± 0.054	1.9	–	11.3	–
37	B2-MM4	–	0.103 ± 0.018	0.101 ± 0.060	3.0	–	0.8	–
38	B2-MM6	0.523 ± 0.296	0.220 ± 0.026	0.081 ± 0.047	13.6	25.0	25.8	$+10.6$
41	B2-MM9	1.021 ± 0.394	0.240 ± 0.026	0.085 ± 0.051	13.7	18.6	33.8	-10.4
43	B2-MM13	0.242 ± 0.049	0.213 ± 0.027	0.079 ± 0.043	18.9	21.4	15.2	$+8.7$
44	B2-MM14	0.310 ± 0.044	0.319 ± 0.035	0.069 ± 0.038	23.6	19.7	40.7	-24.9
45	B2-MM15	0.164 ± 0.020	0.196 ± 0.028	0.071 ± 0.042	6.8	7.3	20.3	-12.3
46	B2-MM16	0.057 ± 0.005	0.100 ± 0.018	0.092 ± 0.050	10.5	7.3	0.7	$+3.4$
48	C-MM3	0.157 ± 0.011	0.301 ± 0.038	0.084 ± 0.055	2.6	3.3	21.2	-17.2
49	C-MM6a	0.101 ± 0.011	0.195 ± 0.029	0.085 ± 0.058	0.4	1.1	7.1	-5.3
50	C-MM6b	0.148 ± 0.022	0.295 ± 0.037	0.091 ± 0.063	0.4	1.3	12.2	-10.0
53	E-MM2d	0.056 ± 0.004	0.218 ± 0.034	0.134 ± 0.088	1.2	1.6	7.2	-5.2
58	F-MM1	0.027 ± 0.005	0.224 ± 0.041	0.139 ± 0.097	0.5	0.7	0.9	$+0.0$
70	H-MM1	–	0.148 ± 0.018	0.223 ± 0.124	5.8	–	2.2	–

in Table 5, but are excluded from Fig. 11 in order to aid comparison with Fig. 10.

Fig. 11 shows that there is no correlation between observed mass and critical BE mass, indicating that, as would be expected for a set of virially unstable cores, our cores cannot be modelled as static, critically-stable, BE spheres. Moreover, the critical BE stability criterion does not reliably predict the either virially bound state or the energy balance of the N_2H^+ cores. A core lying to the right of the line of unity on Fig. 11 has no stable BE solution and must, according to BE analysis, be collapsing under its own gravity, while a core lying to the left of the line of unity may be modelled as a stable, pressure-confined BE sphere.

We find that the BE criterion typically overpredicts the degree to which our cores are gravitationally unstable. Of the 15 cores predicted to be collapsing under gravity according to Fig. 11, 9 are in fact found to pressure-confined. However, there are no cases where the BE analysis suggests a core is pressure-confined and it is found to in fact be gravitationally bound. The degree to which cores are virially bound is in many cases also overestimated. For example, the BE criterion predicts that all six of the cores in Oph B2 will be strongly gravitationally bound, whereas Fig. 10 shows

that of these six cores, four are approximately virialized, and the other two, while virially bound, are confined by external pressure.

A possible explanation for these discrepancies is that in this analysis we have used the standard BE mass formula (equation 41), which does not account for the contribution of non-thermal motion to internal support. However, as shown in Fig. 9, our cores typically have transonic or mildly supersonic internal motions at the radii traced by N_2H^+, and hence assuming all support against collapse is thermal is likely to overestimate the degree to which our cores are both gravitationally unstable and virially bound. An accurate parametrization of the effect of non-thermal internal motion on core support might improve the accuracy of the BE analysis.

Another important consideration is that while in principle the eight cores lying to the left of the line of unity in Fig. 11 can be modelled as stable, pressure-confined BE spheres, Fig. 10 shows that many of our cores, whether confined by pressure or by gravity, are not in virial equilibrium. Caution must be exercised when applying an equilibrium model such as a BE sphere to a non-equilibrium set of objects such as the cores in this sample.
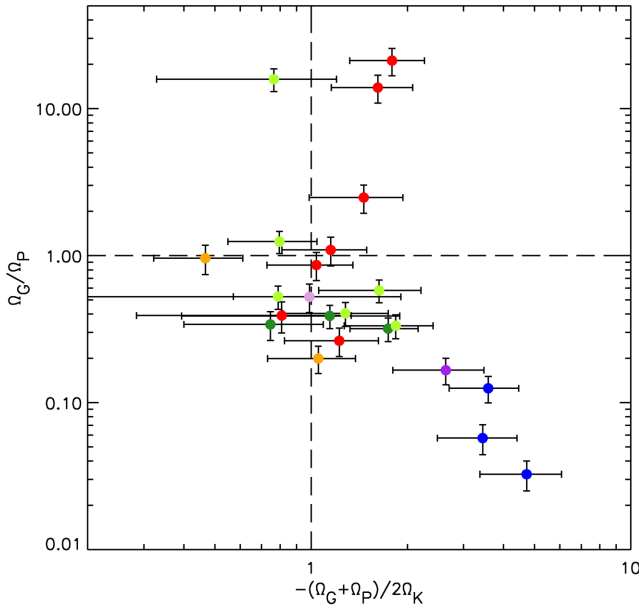
Figure 10. Virial stability of the 23 cores in our catalogue for which N_2H^+ data are available, compared to the ratio of gravitational energy and external pressure terms in the virial equation. The vertical dashed line indicates the line of virial stability, with the right-hand side of the plot being bound and the left-hand side being unbound. The horizontal dashed line marks equipartition between external pressure energy and gravitational potential energy; cores above the line are gravitationally bound, while cores below the line are pressure-confined. Colour coding is as in Fig. 5.
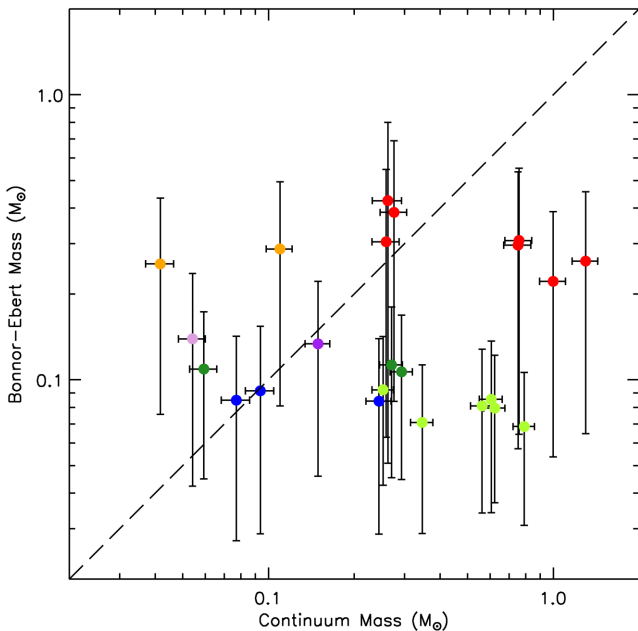
Figure 11. Comparison of continuum-derived mass and BE critical mass for the 23 cores for which N_2H^+ data are available. Cores to the right of the dashed line are collapsing according to the critical Bonner–Ebert criterion. Colour coding is as in Fig. 5.

6 REGIONAL VARIATIONS IN CORE PROPERTIES

Fig. 10 shows that most of the cores in our sample for which N_2H^+ data are available are either bound or virialized. Fig. 5 shows that our cores occupy the part of the mass/size plane in which prestellar cores are expected to lie. However, whether our cores are gravitationally bound (i.e. prestellar) or pressure-confined varies from region to region. Gravity strongly dominates over external pressure in the most massive cores in Oph A, the well-known prestellar cores SM1, SM1N, and SM2. Cores in Oph A′ and B are typically in approximate equipartition between gravitational and pressure energy or marginally pressure dominated. However, cores in Oph C and E are strongly pressure-dominated and virially bound.

It is noticeable from all of the above that the properties of the starless cores, including the degree to which cores are bound, as well as whether they are gravitationally bound or pressure-confined, and the extent to which turbulence is dissipated, vary more between regions than within them. This suggests that the local environment has a significant effect on the nature of the starless cores. Enoch et al. (2009) provide a catalogue of deeply embedded Class 0 and Class I protostars in L1688 and L1689, marked as yellow stars on Fig. 1. We refer to this catalogue in the following discussion.

6.1 Oph A

Oph A is the only region in L1688 within which substantially gravitationally bound cores are found (see Fig. 10). Temperatures in Oph A are higher than in other parts of the cloud. The Oph A region is also the part of the cloud most clearly being influenced by stars that have already formed: the B2 protostar HD 147889 drives a PDR at the western edge of Oph A, while on the eastern side of Oph A there is a reflection nebula associated with the B4 protostar S1, both of which can be seen in Fig. B1. This suggests a morphology in the region in which the dense gas that makes up the central, submillimetre-bright cores of Oph A is being influenced by its local environment. However, as shown in Fig. 10, cores in the densest regions of Oph A do not appear to be dominated by external pressure. Enoch et al. (2009) list only one protostar embedded in Oph A: the Class 0 protostar VLA 1623 (the only Class 0 source in L1688). This is consistent with star formation in this dense clump being in its early stages.

6.2 Oph A′

The cores in Oph A′ are at similar temperatures to those in Oph A, but are among the least bound of the cores in our sample. Gravity and external pressure appear to be contributing approximately equally to the confinement of these cores. This region is confused, particularly along its western edge, where much of the emission is from the PDR associated with HD 147889. Enoch et al. (2009) list three embedded Class I protostars in Oph A′.

6.3 Oph B

The Oph B region appears to be relatively quiescent: it is the coldest of the regions; there are few embedded protostars; and the cores are typically virialized or marginally bound. Enoch et al. (2009) list four embedded Class I protostars in Oph B: none in Oph B1; one in Oph B1B2; and three in Oph B2, of which one is the outflow-driving source IRS 47 (White et al. 2015). Cores in Oph B1 and

B2 typically show similar behaviour, although the ratio of gravitational to pressure energy is consistently in the range 0.3–0.4 in B1, and more varied in B2. As shown in Fig. 9, cores in B2 have the highest non-thermal linewidths measured in N_2H^+, suggesting that turbulence is not being effectively dissipated in this region. We hypothesise that this could be due to the influence of the outflow from IRS 47, as protostellar outflows have been shown to inject and sustain turbulence on small scales in molecular clouds (Duarte-Cabral et al. 2012).

We note that the pre-brown dwarf candidate Oph B-11 (Pound & Blitz 1995; Greaves, Holland & Pound 2003; André, Ward-Thompson & Greaves 2012), located between Oph B1 and B2, is detected in SCUBA-2 850 μm emission. Oph B-11 is discussed in detail in Appendix D.

6.4 Oph C

Oph C appears to be extremely quiescent, and substantially less evolved than the rest of the Oph C–E–F 'filament' of which it appears to be a part. The three cores we identify within Oph C are all substantially bound and pressure-confined, with broad $C^{18}O$ linewidths, as shown in Fig. 9. The N_2H^+ linewidths, however, indicate that the cores in Oph C are among the least supersonic in N_2H^+. The reason for this apparently very effective dissipation of turbulence is not clear, although the lack of embedded sources driving outflows might be a possibility. The lack of embedded sources in Oph C, along with its considerably lower aspect ratio than its neighbours Oph E and Oph F, lead us to suggest that Oph C may have a slightly different line-of-sight distance than other regions, possibly being further from influences such as HD 147889. There are no embedded protostars in Oph C listed by Enoch et al. (2009).

6.5 Oph E and F

We consider Oph E and Oph F together, due to the low number of cores detected in these regions, along with the similarities between the two regions. These appear to be the most evolved regions of L1688, with a high ratio of embedded sources to starless cores: Oph E has four embedded Class I sources, while Oph F has six. Cores in Oph F are at a similar temperature to those in Oph A and A′, although without any obvious external heating. The core in Oph F for which an energy balance can be determined appears to be marginally pressure-confined, while the core in Oph E is strongly pressure-confined. $C^{18}O$ linewidths show substantial turbulence, similarly to Oph C, while these cores are the least supersonic in N_2H^+. Again, we hypothesise that this effective dissipation of turbulence may be the result of a lack of outflows in either of these regions.

6.6 L1689 and L1709

The starless cores we find in L1689 and L1709 are typically of similar mass to those in Oph B, C and E. We find six starless cores in L1689S; four in L1689; and one in L1709. Enoch et al. (2009) list four embedded Class I protostars in L1689S; one Class 0 source in L1689N; and two Class I sources in L1709. The low number of cores relative to L1688, the low ratio of embedded sources to starless cores, and the presence of the Class 0 source IRAS 16293−2422 suggests that L1689 and L1709 are likely to be less evolved than, or forming stars less efficiently than, L1688. This was explained by NWA06 as due to L1689 being further from the Sco OB2 association than L1688, and hence less active.

6.7 Gradients across the cloud

It is clear from the discussion above that the different regions of the L1688 cloud do not show the same properties or evolutionary stage, despite being in close proximity both to one another and to HD 147889. There is a marked variation in temperature across the cloud, with Oph A and A′ being the warmest regions, followed by Oph F, E, C, B1, and B2, in that order. Oph A and A′ are clearly being influenced by the nearby B stars. As discussed in Section 5.3, the flux of ionizing photons from the two B stars is not a dominant term in the virial equation in Oph A. However, these stars will be heating the gas and dust within Oph A.

Fig. 12 shows in blue the warm dust traced by *Spitzer* 8 μm emission (Evans et al. 2003; Enoch et al. 2009), which surrounds Oph A and A′ on two sides. It should be noted that while the relative influence of HD 147889 on L1688 as a whole must be much greater than that of S1, the flux of ionizing photons from S1 on Oph A is approximately twice that of HD 147889; the S1 reflection nebula is likely to have at least as much influence on Oph A as the PDR driven by HD 147889, even though the former is much smaller.

Oph A and Oph B appear to be at similar evolutionary stages, despite their marked difference in temperature. Both regions have embedded sources driving outflows, which may be hindering the dissipation of turbulence within the region. However, while Oph A shows the influence of local effects, Oph B appears to be evolving in a more quiescent location: it is the coldest of the regions, and Fig. 12 shows no sign of it being bordered by PDRs or reflection nebulae.

Cores in Oph A and Oph B are typically of similar mass (see Fig. 8). However, as shown in Fig. 10, while some of the cores in Oph A are strongly gravitationally dominated, the cores in Oph B are close to equipartition between gravitational potential energy and pressure. It is possible that material in Oph A might have been swept up by the PDR and the reflection nebula, increasing local density and hence leading to the strongly gravitationally bound prestellar cores in this region.

Oph E and F appear to be at a later evolutionary stage than Oph A and B, with a high ratio of protostars to starless cores, several embedded sources, and no embedded sources young enough to be driving outflows. Those starless cores that are found are among the least massive in L1688 (see Fig. 8). These regions are both at an intermediate temperature. There is no obvious source of external heating, similarly to Oph B, suggesting that the embedded sources in Oph E and F might be heating their surroundings. What might have led these regions to begin forming stars earlier than Oph A and B is not clear.

Oph C is noticeably different from the other regions in L1688, being an apparently entirely quiescent region, with only a few low-mass, pressure-confined cores and no embedded sources. As discussed above, this leads us to suggest that Oph C might be at a slightly different line-of-sight distance than the neighbouring regions.

There appears to be a general gradient in evolutionary stage from south-west to north-east across the cloud (except for Oph C). This could be due to the influence of the Sco OB2 association, located behind and to the south-west of Ophiuchus (Mamajek 2008); HD 147889, also behind Ophiuchus (Liseau et al. 1999), appears to be primarily of importance in Oph A, and to have relatively limited influence elsewhere.

While a global south-west/north-east gradient in evolutionary stage can be inferred, and is consistent with previous studies (Loren 1989; NWA06), it must be emphasized that the properties of
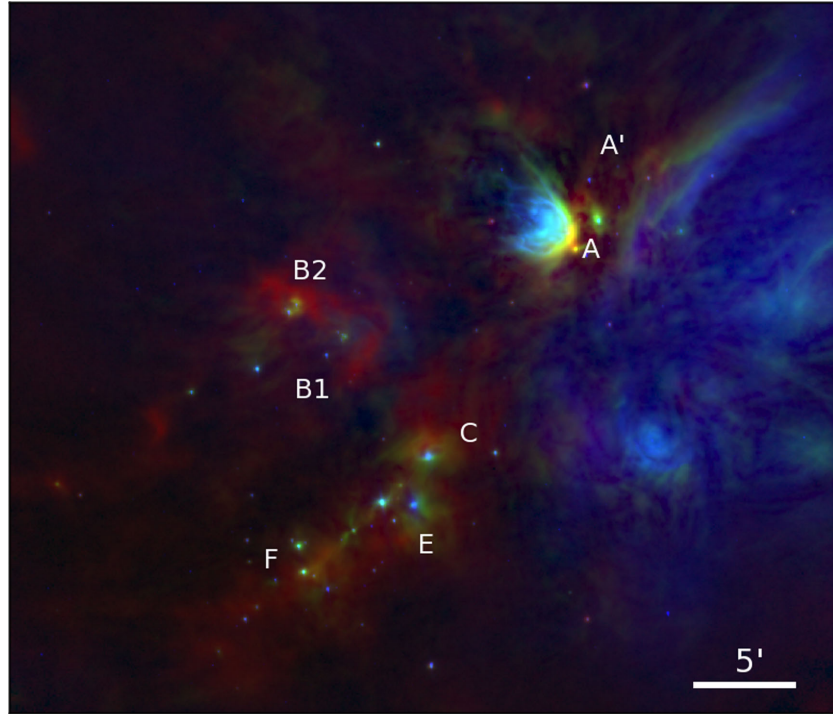
Figure 12. Three-colour image of L1688, with regions labelled. Red channel: SCUBA-2 850 μm data (this work). Green channel: *Herschel* 100 μm data (Ladjelate et al., in preparation). Blue channel: *Spitzer* 8 μm data (Evans et al. 2003).

regions within L1688 appear to be determined substantially by local effects. In particular, the differences in temperature and energy balance between cores in Oph A and Oph B, two regions apparently at similar evolutionary stages, but with different immediate local environments (Oph A being heavily influenced by two B stars, and Oph B evolving in a less disturbed location), indicate the importance of local effects in determining the properties of starless cores.

7 CONCLUSIONS

In this paper, we have extracted a set of sources from the SCUBA-2 850 μm map of the Ophiuchus molecular cloud, and have characterized the properties of these cores using SCUBA-2, *Herschel*, IRAM, and HARP data sets.

We identified sources using the CuTEx curvature-based source extraction algorithm, which gave us a catalogue of 93 sources, 70 of which were in the central region of the L1688 subcloud. Of these 93 sources, 46 were identified as protostellar, and 47 were identified as starless cores. Of the 70 sources in L1688, 47 were uniquely identified with a source in the S08 catalogue.

We determined the dust temperature of each source by SED fitting, which allowed an accurate mass determination to be made for each source. The distribution of masses of the starless cores is consistent with the expected shape of the CMF. The low counting statistics of our sample did not allow us to accurately determine the power-law index of our CMF, although the two slope values determined, $\alpha = 2.0 \pm 0.4$ and 2.7 ± 0.4 are both consistent with the expected behaviour of the high-mass IMF.

We calculated the masses of our cores from N_2H^+ and $C^{18}O$ emission. We found that the mass of a core determined from 850-μm continuum emission and the mass determined from N_2H^+ emission correlate well, indicating that N_2H^+ and continuum emission are tracing the same material. The most massive cores, those in Oph

A, have consistently higher continuum masses than N_2H^+ masses, indicating that as expected, N_2H^+ emission does not trace the very densest material in prestellar cores.

We performed full virial stability analyses for the 23 cores for which both $C^{18}O$ and N_2H^+ data were available, estimating the contributions of gravitational energy, internal pressure (both thermal and non-thermal) and external pressure to the energy balance of the cores. Existing measurements of the magnetic field strength in Ophiuchus suggest that magnetic energy is unlikely to significantly alter the energy balance of our cores. We found that most of our cores are bound or virialized, with a virial ratio ≥ 1.

We calculated the BE critically stable masses for each of the 23 cores for which N_2H^+ data are available. We found that our cores cannot be modelled as critically stable BE spheres, and that the BE critically stable mass is not a good estimator of the bound state of the cores for which we can perform a full virial analysis, typically overestimating the degree to which cores are gravitationally bound.

We found that whether our cores are gravitationally bound or pressure-confined depends strongly on the region in which they are located. Cores in the centre of Oph A are gravitationally bound, while cores in Oph C and E are pressure-confined. Cores in Oph A′, B, and F are in approximate equipartition between gravitational potential energy and external pressure energy, with pressure typically slightly dominating.

We see a loss of turbulence between core linewidths measured in $C^{18}O$ and core linewidths measured in N_2H^+. This supports a picture in which dissipation of turbulence occurs in the dense centres of starless cores. At the radii traced by N_2H^+ emission, turbulence is dissipating, but is not yet fully dissipated, with a transonic or mildly supersonic non-thermal component to the core linewidth still present even when the core is on the brink of gravitational collapse. The degree to which turbulence is dissipated varies between regions,

with turbulence being dissipated more within Oph C, E, and F than within Oph A, A′, and B.

These results show that starless cores in the Ophiuchus molecular cloud are non-equilibrium objects with complex relationships with their local environments, and that a detailed analysis of their energy balance, of the sort we have carried out here, is required in order to accurately determine their virial state. In particular, we have shown that external pressure is of key importance to the energy balance of most of the densest starless cores in Ophiuchus, and thus cannot be neglected in a virial analysis. The wealth of continuum and kinematic data now available for many galactic star-forming regions now allows for detailed analyses of the virial balance of starless cores in other regions to be performed, and a thorough understanding of their behaviour and relationship with their environments to be developed. In future papers, we will carry out such studies in other Gould Belt star-forming regions.

REFERENCES

Alves J. F., Lada C. J., Lada E. A., 2001, Nature, 409, 159
André P., Montmerle T., 1994, ApJ, 420, 837
André P., Ward-Thompson D., Barsony M., 1993, ApJ, 406, 122
André P., Belloche A., Motte F., Peretto N., 2007, A&A, 472, 519
André P. et al., 2010, A&A, 518, L102
André P., Ward-Thompson D., Greaves J., 2012, Science, 337, 69
André P., Di Francesco J., Ward-Thompson D., Inutsuka S.-I., Pudritz R. E., Pineda J., 2014, in Beuther H., Klessen R. S., Dullemond C. P., Henning T., eds, Protostars and Planets VI. Univ. Arizona Press, Tucson, AZ, p. 27
Aniano G., Draine B. T., Gordon K. D., Sandstrom K., 2011, PASP, 123, 1218
Basu S., 2000, ApJ, 540, L103
Beckwith S. V. W., Sargent A. I., Chini R. S., Guesten R., 1990, AJ, 99, 924
Bintley D. et al., 2014, in Holland W. S., Zmuidzinas J., eds, Proc. SPIE Conf. Ser. Vol. 9153, Millimeter, Submillimeter, and Far-Infrared Detectors and Instrumentation for Astronomy VII. SPIE, Bellingham, p. 915303
Bonnor W. B., 1956, MNRAS, 116, 351
Bontemps S. et al., 2001, A&A, 372, 173
Buckle J. V. et al., 2009, MNRAS, 399, 1026
Buckle J. V. et al., 2010, MNRAS, 401, 204
Caselli P., Walmsley C. M., Zucconi A., Tafalla M., Dore L., Myers P. C., 2002, ApJ, 565, 344
Chabrier G., 2003, PASP, 115, 763
Chapin E. L., Berry D. S., Gibb A. G., Jenness T., Scott D., Tilanus R. P. J., Economou F., Holland W. S., 2013, MNRAS, 430, 2545
Christie H. et al., 2012, MNRAS, 422, 968
Crutcher R. M., Troland T. H., Goodman A. A., Heiles C., Kazes I., Myers P. C., 1993, ApJ, 407, 175
Daniel F., Cernicharo J., Dubernet M.-L., 2006, ApJ, 648, 461
Dempsey J. T. et al., 2013, MNRAS, 430, 2534
Di Francesco J., André P., Myers P. C., 2004, ApJ, 617, 425
Di Francesco J., Evans N. J. I., Caselli P., Myers P. C., Shirley Y., Aikawa Y., Tafalla M., 2007, in Reipurth B., Jewitt D., Tucson K. K., eds, Protostars and Planets V. Univ. Arizona Press, Tuscon, AZ, p. 17
Dolidze M. V., Arakelyan M. A., 1959, Astron. Zh., 36, 444
Dottori H. A., 1980, Ap&SS, 73, 175
Drabek E. et al., 2012, MNRAS, 426, 23
Duarte-Cabral A., Chrysostomou A., Peretto N., Fuller G. A., Matthews B., Schieven G., Davis G. R., 2012, A&A, 543, A140
Ebert R., 1955, Z. Astrophys., 37, 217
Elmegreen B. G., Falgarone E., 1996, ApJ, 471, 816
Emerson D., 1999, Interpreting Astronomical Spectra. Wiley-VCH, New York
Enoch M. L., Evans N. J. I., Sargent A. I., Glenn J., Rosolowsky E., Myers P., 2008, ApJ, 684, 1240
Enoch M. L., Evans N. J., II, Sargent A. I., Glenn J., 2009, ApJ, 692, 973
Evans N. J., II, et al., 2003, PASP, 115, 965
Evans N. J., II, et al., 2009, ApJS, 181, 321
Frerking M. A., Langer W. D., Wilson R. W., 1982, ApJ, 262, 590
Friesen R. K., Di Francesco J., Shimajiri Y., Takakuwa S., 2010, ApJ, 708, 1002
Fuller G. A., Myers P. C., 1992, ApJ, 384, 523
Garden R. P., Hayashi M., Hasegawa T., Gatley I., Kaifu N., 1991, ApJ, 374, 540
Goodman A. A., Heiles C., 1994, ApJ, 424, 208
Goodman A. A., Barranco J. A., Wilner D. J., Heyer M. H., 1998, ApJ, 504, 223
Gould B. G., 1879, Resultados Obs. Nac. Argentino, Vol. 1. P. E. Coni., Buenos Aires
Greaves J. S., Holland W. S., Pound M. W., 2003, MNRAS, 346, 441
Greene T. P., Young E. T., 1992, ApJ, 395, 516
Greene T. P., Wilking B. A., André P., Young E. T., Lada C. J., 1994, ApJ, 434, 614
Griffin M. J. et al., 2010, A&A, 518, L3
Herschel Sir J. F. W., 1847, Results of astronomical observations made during the years 1834, 5, 6, 7, 8 at the Cape of Good Hope. Smith, Elder and Co., London
Hildebrand R. H., 1983, QJRAS, 24, 267
Holland W. S. et al., 2013, MNRAS, 430, 2513
Johnson R. D. I., 2013, Available at: http://cccbdb.nist.gov/, release 16a
Johnstone D., Wilson C. D., Moriarty-Schieven G., Joncas G., Smith G., Gregersen E., Fich M., 2000, ApJ, 545, 327
Kirk J. M. et al., 2013, MNRAS, 432, 1424
Klessen R. S., Ballesteros-Paredes J., Vázquez-Semadeni E., Durán-Rojas C., 2005, ApJ, 620, 786
Koen C., 2006, MNRAS, 365, 590
Könyves V. et al., 2010, A&A, 518, L106
Kroupa P., 2001, MNRAS, 322, 231
Leous J. A., Feigelson E. D., André P., Montmerle T., 1991, ApJ, 379, 683
Liseau R. et al., 1999, A&A, 344, 342
Loren R. B., 1989, ApJ, 338, 902
Mamajek E. E., 2008, Astron. Nachr., 329, 10
Markwardt C. B., 2009, in Bohlender D. A., Durand D., Dowler P., eds, ASP Conf. Ser. Vol. 411, Astronomical Data Analysis Software and Systems XVIII. Astron. Soc. Pac., San Francisco, p. 251
Maruta H., Nakamura F., Nishi R., Ikeda N., Kitamura Y., 2010, ApJ, 714, 680
Maschberger T., Kroupa P., 2009, MNRAS, 395, 931
Mizuno A., Fukui Y., Iwata T., Nozawa S., Takano T., 1990, ApJ, 356, 184
Molinari S., Schisano E., Faustini F., Pestalozzi M., di Giorgio A. M., Liu S., 2011, A&A, 530, A133
Motte F., André P., Neri R., 1998, A&A, 336, 150 (MAN98)
Motte F., André P., Ward-Thompson D., Bontemps S., 2001, A&A, 372, L41
Müller H. S. P., Thorwirth S., Roth D. A., Winnewisser G., 2001, A&A, 370, L49
Nutter D., Ward-Thompson D., 2007, MNRAS, 374, 1413
Nutter D., Ward-Thompson D., André P., 2006, MNRAS, 368, 1833 (NWA06)

Offner S. S. R., Klein R. I., McKee C. F., 2008, ApJ, 686, 1174

Pilbratt G. L. et al., 2010, A&A, 518, L1

Pineda J. E., Caselli P., Goodman A. A., 2008, ApJ, 679, 481

Pineda J. E., Goodman A. A., Arce H. G., Caselli P., Foster J. B., Myers
P. C., Rosolowsky E. W., 2010, ApJ, 712, L116

Pirogov L., Zinchenko I., Caselli P., Johansson L. E. B., Myers P. C., 2003,
A&A, 405, 639

Planck VI, 2011, A&A, 536, A6

Poglitsch A. et al., 2010, A&A, 518, L2

Pound M. W., Blitz L., 1995, ApJ, 444, 270

Quinn C., 2013, PhD thesis, Cardiff University

Roy A. et al., 2014, A&A, 562, A138

Sadavoy S. I. et al., 2010, ApJ, 710, 1247

Sadavoy S. I. et al., 2013, ApJ, 767, 126

Salpeter E. E., 1955, ApJ, 121, 161

Simpson R. J., Nutter D., Ward-Thompson D., 2008, MNRAS, 391, 205
(S08)

Simpson R. J., Johnstone D., Nutter D., Ward-Thompson D., Whitworth
A. P., 2011, MNRAS, 417, 216

Stamatellos D., Whitworth A. P., Ward-Thompson D., 2007, MNRAS, 379,
1390

Strom S. E., Peterson D. M., 1968, ApJ, 152, 859

Swinyard B. M. et al., 2010, A&A, 518, L4

Troland T. H., Crutcher R. M., Goodman A. A., Heiles C., Kazes I., Myers
P. C., 1996, ApJ, 471, 302

Vrba F. J., 1977, AJ, 82, 198

Vrba F. J., Strom K. M., Strom S. E., Grasdalen G. L., 1975, ApJ, 197, 77

Ward-Thompson D., Scott P. F., Hills R. E., André P., 1994, MNRAS, 268,
276

Ward-Thompson D., André P., Kirk J. M., 2002, MNRAS, 329, 257

Ward-Thompson D., Nutter D., Bontemps S., Whitworth A., Attwood R.,
2006, MNRAS, 369, 1201

Ward-Thompson D., André P., Crutcher R., Johnstone D., Onishi T., Wilson
C., 2007, in Reipurth B., Jewitt D., Tucson K. K., eds, Protostars and
Planets V. Univ. Arizona Press, Tucson, AZ, p. 33

Ward-Thompson D. et al., 2007, PASP, 119, 855

Wenger M. et al., 2000, A&AS, 143, 9

White G. J. et al., 2015, MNRAS, 447, 1996

Wilking B. A., Lada C. J., 1983, ApJ, 274, 698

Wilking B. A., Gagné M., Allen L. E., 2008, in Reipurth B., ed., ASP
Monograph Publications, Vol. 5, Handbook of Star Forming Regions,
Volume II: The Southern Sky. Astron. Soc. Pac., San Francisco, CA,
p. 351

Wilson T. L., 1999, Rep. Prog. Phys., 62, 143

Young E. T., Lada C. J., Wilking B. A., 1986, ApJ, 304, L45

APPENDIX A: DATA

We show in full the regions within Ophiuchus observed using
SCUBA-2. Fig. A1 shows the 850-μm flux density data. Fig. A2
shows the 850-μm variance map. Fig. A3 shows the 450-μm flux
density data. Fig. A4 shows the 450-μm variance map. Figs A1–A4
all show the data in square-root scaling. Fig. A5 shows the mask
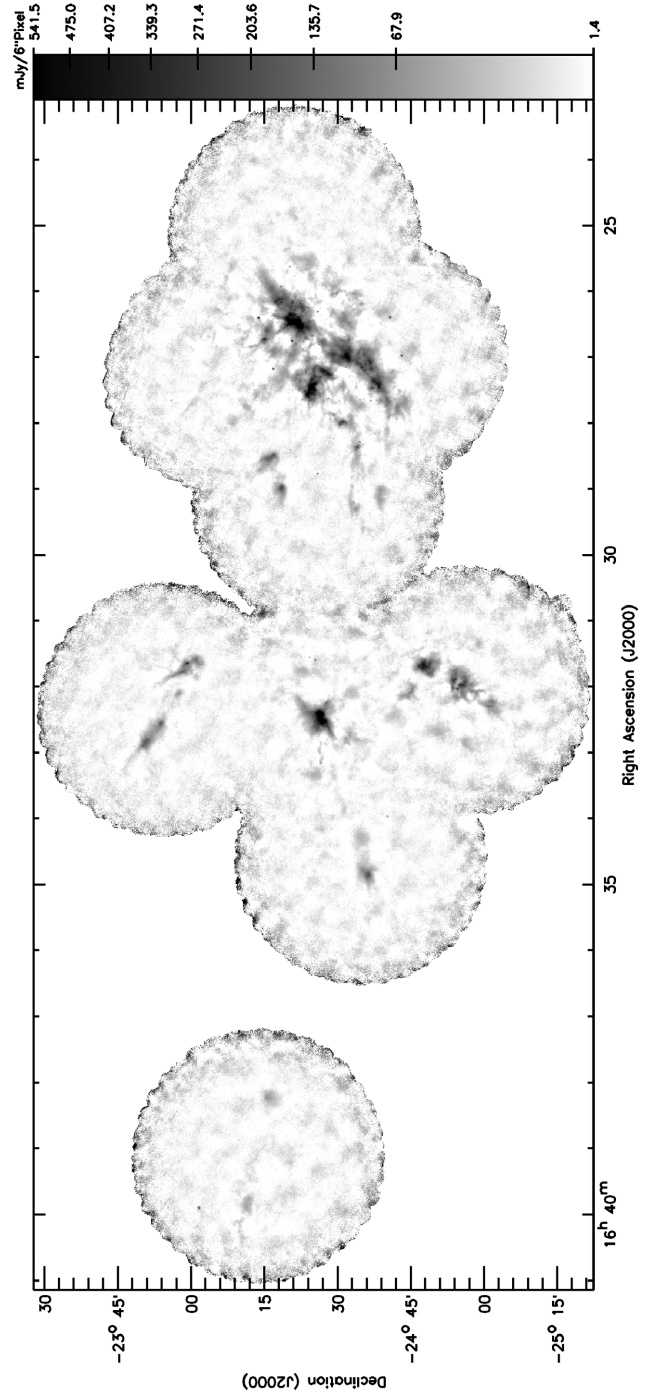used to define areas of significant emission in both the 850 and
450-μm data.

Figure A1. The 850-μm flux density measured in Ophiuchus with SCUBA-
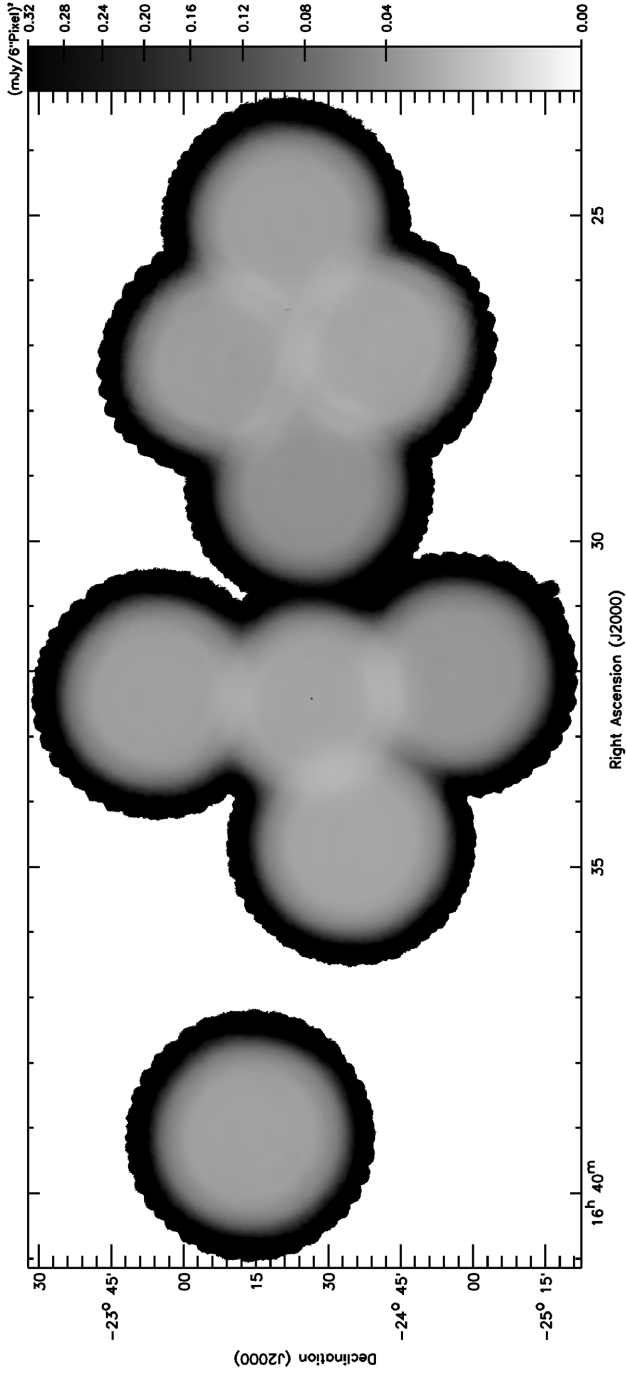2, shown in square-root scaling.

Figure A2. The variance on the SCUBA-2 850-μm flux density data, shown in square-root scaling.
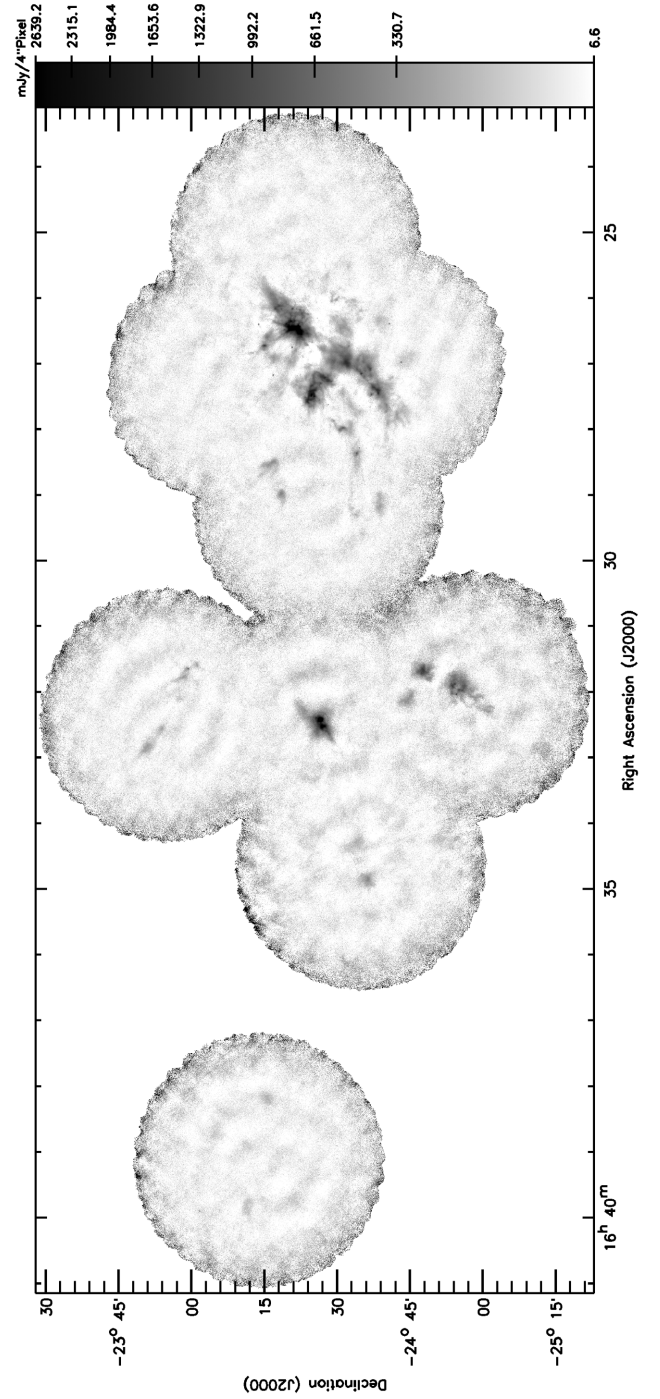

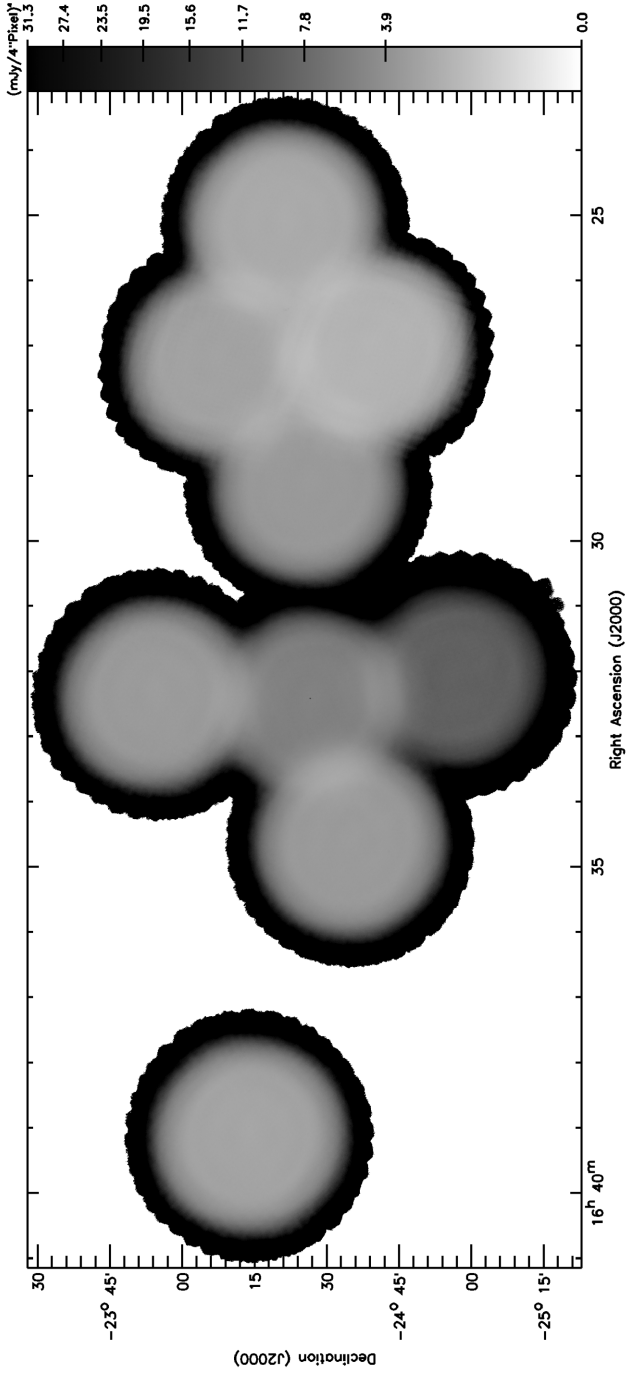**Figure A3.** The 450-μm flux density measured in Ophiuchus with SCUBA-2, shown in square-root scaling.

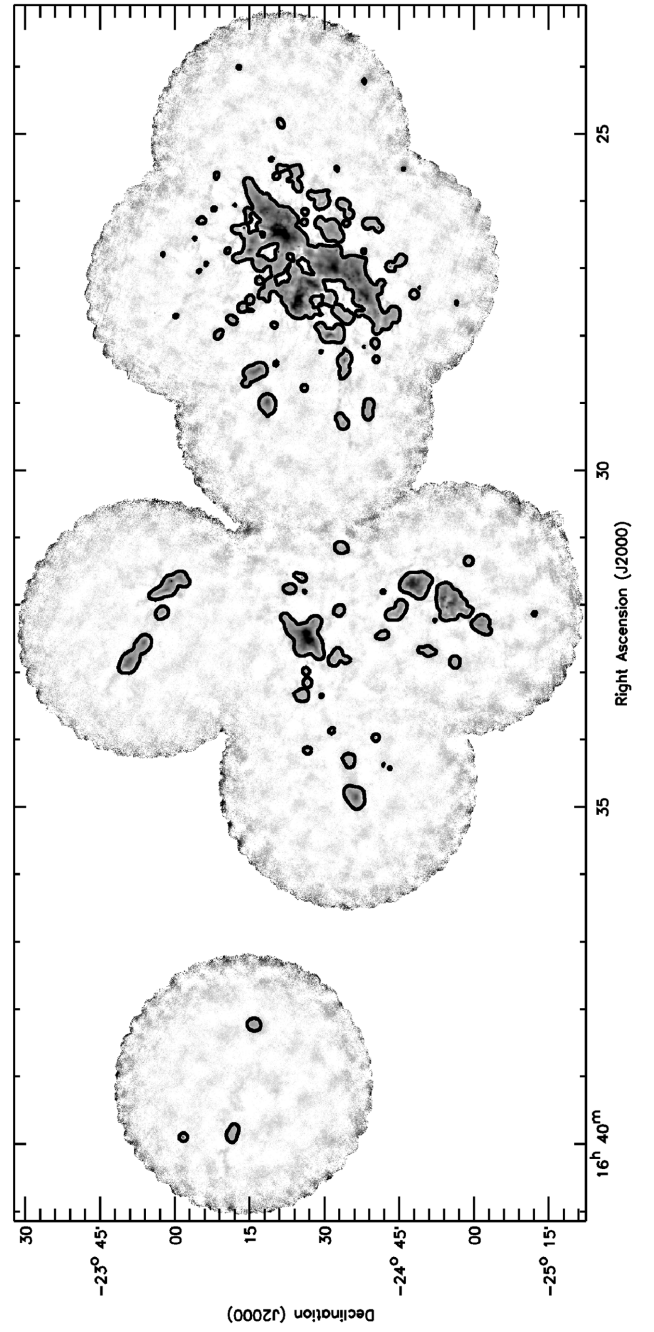**Figure A4.** The variance on the SCUBA-2 450-μm flux density data, shown in square-root scaling.

Figure A5. The mask used in the data reduction process, enclosing regions of significant emission, shown as a thick contour, overlaying the 850-μm flux density data, shown as a grey-scale.

APPENDIX B: RGB IMAGES OF L1688
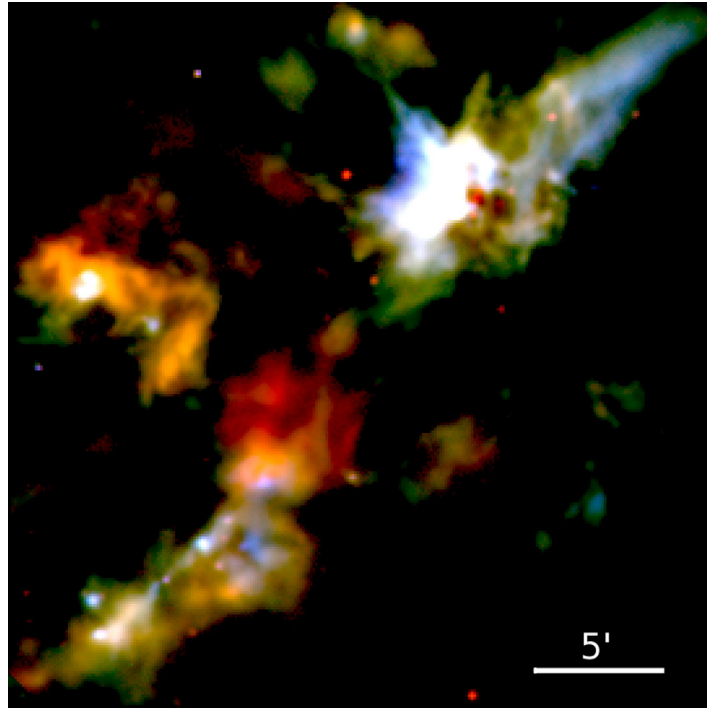
Figure B1. Three-colour image of L1688. Red channel: SCUBA-2 850 μm data. Green channel: spatially-filtered *Herschel* 250 μm data. Blue channel: spatially-filtered *Herschel* 160 μm data.
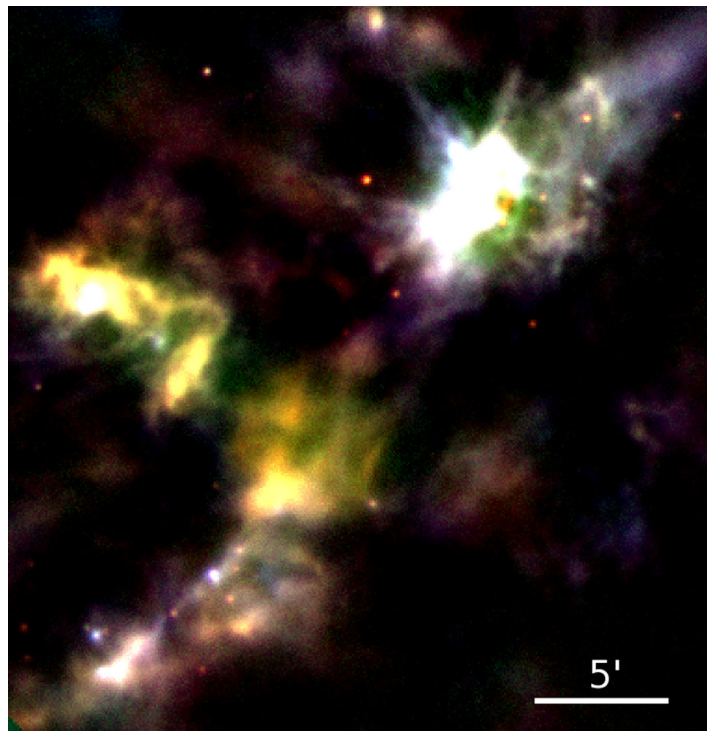
Figure B2. Three-colour image of L1688. Red channel: SCUBA-2 850 μm data. Green channel: SCUBA-2 450 μm data. Blue channel: spatially-filtered *Herschel* 250 μm data.

APPENDIX C: GRAVITATIONAL POTENTIAL ENERGY OF A GAUSSIAN DISTRIBUTION

We give here a brief derivation of the gravitational potential energy of a Gaussian distribution, as used in our virial analysis. This is the first time that this has been shown.

For a radially symmetric potential, the gravitational potential energy Ω_G is given by

$$\Omega_G = -4\pi G \int_0^\infty dr\, r\, \rho(r) M(r), \tag{C1}$$

where $\rho(r)$ and $M(r)$ are the density and mass at radius r, respectively. $M(r)$ is given by

$$M(r) = 4\pi \int_0^r dr'\, r'^2 \rho(r'). \tag{C2}$$

We assume a radially symmetric Gaussian density distribution

$$\rho(r) = \rho_0 e^{-r^2/2\alpha^2}, \tag{C3}$$

for which the total mass at radius r is given by

$$M(r) = 4\pi\rho_0 \int_0^r dr'\, r'^2\, e^{-r'^2/2\alpha^2} \tag{C4}$$

$$= 4\pi\rho_0 \left[\alpha^3 \sqrt{\frac{\pi}{2}} \operatorname{erf}\left(\frac{r}{\alpha\sqrt{2}}\right) - \alpha^2 r e^{-r^2/2\alpha^2} \right], \tag{C5}$$

and the total mass summed over all radii is given by

$$M = 4\pi\rho_0 \int_0^\infty dr'\, r'^2\, e^{-r'^2/2\alpha^2} \tag{C6}$$

$$= 2\sqrt{2}\pi^{3/2}\rho_0\alpha^3. \tag{C7}$$

Using equations (B1) and (B5), Ω_G is given by

$$\Omega_G = -16\pi^2 G \rho_0^2 \alpha^2$$
$$\times \int_0^\infty dr\, r\, e^{-r^2/2\alpha^2} \left[\alpha\sqrt{\frac{\pi}{2}} \operatorname{erf}\left(\frac{r}{\alpha\sqrt{2}}\right) - r e^{-r^2/2\alpha^2} \right] \tag{C8}$$

$$= -16\pi^2 G \rho_0^2 \alpha^2 \times \left(\frac{\alpha^3\sqrt{\pi}}{4}\right) \tag{C9}$$

$$= -4\pi^{5/2} G \rho_0^2 \alpha^5. \tag{C10}$$

Combining equations (B7) and (B10), the gravitational potential energy of a Gaussian distribution of characteristic width α and total mass M is

$$\Omega_G = -\frac{1}{2\sqrt{\pi}} \frac{GM^2}{\alpha}. \tag{C11}$$

This is used in equation (30) in Section 5.1 in the text.

APPENDIX D: OPH B-11

We investigated whether the pre-brown dwarf source Oph B-11 was detectable in our 850-μm map of Ophiuchus. Originally detected and identified as a pre-brown dwarf candidate in a DCO$^+$ search (Pound & Blitz 1995), Oph B-11 was observed using SCUBA by Greaves et al. (2003), who classed the source as a very young 'isolated planet'. André et al. (2012) observed Oph B-11 using the IRAM Plateau de Bure Interferometer, determining that the source was in fact a gravitationally bound pre-brown dwarf, with mass 0.02–0.03 $M_\odot$.
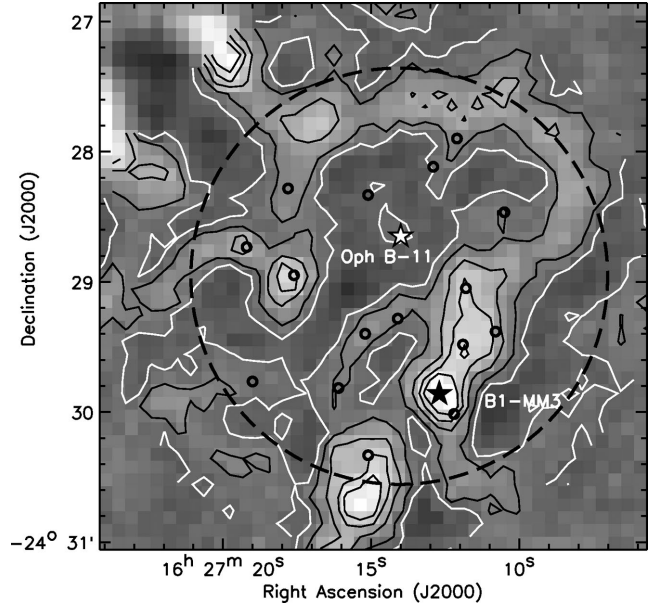

Figure D1. Unsharp-masked SCUBA-2 850 μm image of the region surrounding Oph B-11, smoothed to 15 arcsec resolution. Our peak position for Oph B-11 is marked as a white star. B1-MM3 is marked as a black star. Other sources identified by Greaves et al. (2003) are marked as black circles. The approximate area observed by Greaves et al. (2003) is enclosed by the dashed line. Contour levels are 28, 66, 94, 115 and 129 mJy (15 arcsec beam)$^{-1}$ above the local minimum, to approximately match the contours of Greaves et al. (2003).

When observed by Greaves et al. (2003), the integration time for the 2.7 arcmin diameter field was 2 h, resulting in a very sensitive SCUBA map with 1σ rms noise of 6 mJy (15 arcsec beam)$^{-1}$. The 1σ rms noise in our SCUBA-2 map of the same region is 6.3 mJy (15 arcsec beam)$^{-1}$, almost identical. This was achieved using $4 \times$ PONG1800 observations, taking a total of 2 h 40 min (i.e. essentially the same integration time as with SCUBA) to cover a field of 30 arcmin diameter, compared to 2.7 arcmin with SCUBA (i.e. roughly 120 times the area in the same time).

In order to detect this extremely faint source, we repeated the unsharp-masking process used by Greaves et al. (2003) on their SCUBA map of the region. We smoothed the SCUBA-2 map with a 30 arcsec Gaussian filter, and subtracted the smoothed emission from the original map, removing all structure significantly more extended than the 14.1 arcsec beam. The data were them smoothed to a 15 arcsec beam to match the SCUBA data of Greaves et al. (2003).

After removing the extended structure in this way from the SCUBA-2 map, we were able to detect Oph B-11. The emission peaks at RA $= 16^h27^m14\overset{s}{.}0$, Dec. $= -24°28'39''$. Greaves et al. (2003) found the source position to be RA $= 16^h27^m14\overset{s}{.}0$ Dec. $= -24°28'31''$, while André et al. (2012) give the source position as R.A. $= 16^h27^m13\overset{s}{.}96$ Dec. $= -24°28'29\overset{''}{.}3$. All of these positions are consistent within the quoted errors.

We measure a peak flux density above the local background for Oph B-11 of 55 ± 6 mJy (15 arcsec beam)$^{-1}$ with an uncertainty on the local background of ± 9 mJy (15 arcsec beam)$^{-1}$. Greaves et al. (2003) find a peak 850-μm flux density for Oph B-11 of 39 ± 6 mJy (15 arcsec beam)$^{-1}$, with an uncertainty on their local background of ± 5 mJy (15 arcsec beam)$^{-1}$. Thus, our measurement of the peak flux density of Oph B-11 is consistent with that of Greaves et al. (2003). We converted our peak flux density to a mass

using the Greaves et al. ([2003](#)) temperature estimate of 12–20 K, taking $\kappa_{850\,\mu m} = 0.01$ cm^2 g^{-1}, and assuming a distance of 138 pc. We find a mass range for Oph B-11 of 0.011–0.024 M$_\odot$. Thus, our data are consistent with the IRAM mass estimate (André et al. [2012](#)), and hence with the pre-brown dwarf interpretation of Oph B-11.

[1]*Jeremiah Horrocks Institute, University of Central Lancashire, Preston, Lancashire PR1 2HE, UK*

[2]*Department of Physical Sciences, The Open University, Milton Keynes MK7 6AA, UK*

[3]*The Rutherford Appleton Laboratory, Chilton, Didcot OX11 0NL, UK*

[4]*Imperial College London, Blackett Laboratory, Prince Consort Rd, London SW7 2BB, UK*

[5]*Astrophysics Group, Cavendish Laboratory, J J Thomson Avenue, Cambridge CB3 0HE, UK*

[6]*Kavli Institute for Cosmology, Institute of Astronomy, University of Cambridge, Madingley Road, Cambridge CB3 0HA, UK*

[7]*Department of Physics and Astronomy, University of Waterloo, Waterloo, Ontario N2L 3G1, Canada*

[8]*Joint Astronomy Centre, 660 N. A'ohōkū Place, University Park, Hilo, Hawaii 96720, USA*

[9]*Department of Physics and Astronomy, University of Victoria, Victoria, BC V8P 1A1, Canada*

[10]*Physics and Astronomy, University of Exeter, Stocker Road, Exeter EX4 4QL, UK*

[11]*NRC Herzberg Astronomy and Astrophysics, 5071 West Saanich Rd, Victoria, BC V9E 2E7, Canada*

[12]*Department of Astronomy, Cornell University, Ithaca, NY 14853, USA*

[13]*Leiden Observatory, Leiden University, PO Box 9513, NL-2300 RA Leiden, the Netherlands*

[14]*School of Physics and Astronomy, Cardiff University, The Parade, Cardiff CF24 3AA, UK*

[15]*European Southern Observatory (ESO), Karl-Schwarzschild-Straße 2, D-85748 Garching bei München, Germany*

[16]*Jodrell Bank Centre for Astrophysics, Alan Turing Building, School of Physics and Astronomy, University of Manchester, Oxford Road, Manchester M13 9PL, UK*

[17]*Institute for Astronomy, ETH Zurich, Wolfgang-Pauli-Strasse 27, CH-8093 Zurich, Switzerland*

[18]*Laboratoire AIM CEA/DSM-CNRS-Université Paris Diderot, IRFU/Service d'Astrophysique, CEA Saclay, F-91191 Gif-sur-Yvette, France*

[19]*Centre de Recherche en Astrophysique du Québec et département de physique, Université de Montréal, C.P. 6128, succ. centre-ville, Montréal, QC H3C 3J7, Canada*

[20]*James Madison University, Harrisonburg, Virginia 22807, USA*

[21]*School of Physics, Astronomy & Mathematics, University of Hertfordshire, College Lane, Hatfield, Herts AL10 9AB, UK*

[22]*Astrophysics Research Institute, Liverpool John Moores University, Egerton Warf, Birkenhead CH41 1LD, UK*

[23]*Department of Physics & Astronomy, University of Manitoba, Winnipeg, MB R3T 2N2 Canada*

[24]*Dunlap Institute for Astronomy & Astrophysics, University of Toronto, 50 St George St, Toronto, ON M5S 3H4, Canada*

[25]*Physics & Astronomy, University of St Andrews, North Haugh, St Andrews, Fife KY16 9SS, UK*

[26]*UK Astronomy Technology Centre, Royal Observatory, Blackford Hill, Edinburgh EH9 3HJ, UK*

[27]*Institute for Astronomy, Royal Observatory, University of Edinburgh, Blackford Hill, Edinburgh EH9 3HJ, UK*

[28]*Centre de recherche en astrophysique du Québec et Département de physique, de génie physique et d'optique, Université Laval, 1045 avenue de la médecine, Québec, G1V 0A6, Canada*

[29]*Institut d'Astrophysique Spatiale, CNRS/Université Paris-Sud 11, F-91405 Orsay, France*

[30]*Department of Physics and Astronomy, UCL, Gower St, London WC1E 6BT, UK*

[31]*Department of Physics and Astronomy, McMaster University, Hamilton, ON L8S 4M1, Canada*

[32]*Department of Physics, University of Alberta, Edmonton, AB T6G 2E1, Canada*

[33]*Max Planck Institute for Astronomy, Königstuhl 17, D-69117 Heidelberg, Germany*

[34]*IFSI - INAF, via Fosso del Cavaliere 100, I-00133 Roma, Italy*

[35]*University of Western Sydney, Locked Bag 1797, Penrith, NSW 2751, Australia*

[36]*National Astronomical Observatory of China, 20A Datun Road, Chaoyang District, Beijing 100012, China*

This paper has been typeset from a TEX/LATEX file prepared by the author.